PROCEEDINGS OF SCIENCE

Review of RPC simulation and modelling

P. Fonte[1]
LIP-Laboratório de Instrumentação e Física Experimental de Partículas
Dep. de Física, Univ. de Coimbra, 3004-516 Coimbra, Portugal
ISEC-Instituto Superior de Engenharia de Coimbra
Rua Pedro Nunes - Quinta da Nora, 3030-199 Coimbra, Portugal
E-mail: fonte@coimbra.lip.pt

In spite of their apparent simplicity, RPCs feature a range of physical situations somewhat more complex than those found in most other gaseous detectors. These include the interplay between materials with different electrical characteristics, space-charge dominated avalanches evolving in very high electric fields and the propagation of fast signals on heterogeneous multiconductor transmission lines. In this article the state-of-the-art of the modelling of many of these aspects is reviewed and some aspects still requiring further work highlighted.

XI workshop on Resistive Plate Chambers and Related Detectors (RPC2012)
INFN-Laboratori Nazionali di Frascati, Italy
February 5-10, 2012

[1] Speaker

PoS(RPC2012)033

PROCEEDINGS OF SCIENCE

1. Introduction

On aiming to review the status of simulation and modelling in RPCs it became apparent that it would be necessary to state some of the basic physics as well: most modelling involves some degree of approximation that can only be properly appreciated if the underlying physics is clear. Furthermore, most problems can only be exactly addressed by a combination of numerical calculations for quantities such as the electric field and Monte Carlo simulations for the stochastic behaviour of the detector under irradiation, which need a correct physical understanding. On the other hand, the results of such purely numerical calculations tend to be hardly generalizable and its features quite opaque, so in here we will privilege analytical treatments whenever available, even if necessarily approximate.

A minimum of RPC technology must as well be stated, as modelling must cover the relevant technical realities of RPC construction.

Although there was a pedagogical concern in the elaboration of this review, in the sense that it may provide an introduction about the fundamentals of RPC physical modelling to students entering the field, it is assumed that the reader has a basic knowledge on the principles of gaseous particle detectors, for which several good reviews are available (e.g. [1]-[4]).

Considerable attention was paid to the unification of results scattered over many publications in a common coherent framework with unified notation. For obvious need of abbreviation, often only the most relevant results were presented and deductions streamlined.

On section 2 are exposed the main technological features that influence the RPC behaviour and require physical modelling.

Section 3 concerns the polarization of the gas gaps, including voltage drops in the various technical elements and stochastic variations caused by the counting process.

A large Section 4 is devoted to the development of avalanches in the swarm approximation. The classical theory of swarms is reviewed and expanded. Closed analytical expressions were derived for almost all quantities of interest regarding diffusive avalanches in the Townsend regime (space-charge free) arising from single electron-ion pairs deposited anywhere within the gas gap, along with the case of uniform ionization. Some results concerning the analytical calculation of the space-charge field are given and the space-charge effect is addressed, both in the form of a numerical example solution and of empirical models. Finally the subject of avalanche growth fluctuations is addressed, both in the Townsend and space-charge regimes, with the help of the models previously mentioned.

Section 5 deals with the signal fluctuations arising in practice owing to the composition of avalanche fluctuations with ionization statistics. These include timing characteristics in the Townsend and (briefly) space-charge regimes and the charge spectrum in the Townsend regime.

Section 6 reviews the theory of signal induction and addresses the problem of the influence of conductive materials.

PoS(RPC2012)033

Section 7 concerns the signal transmission in multistrip readout electrodes, specially important for timing RPCs. The frequency spectrum of the signals is discussed and the multiconductor transmission line theory as applied to RPCs is exposed. The fundamental characteristics are treated in the framework of a weak-coupling approximation that may be particularly adapted to describe RPCs.

Only the state-of-the-art was reviewed and no attempt was made to give the historical perspective. The interested reader may follow the reference chain departing from the quoted articles. Little attention was given to comparisons with measurements, as these are given in the original articles.

1.1. Time scales

In modelling RPC behaviour it is worth noting in advance that there are phenomena occurring in three very different time scales, such that when modelling the faster ones, those occurring at the slower time scales may be considered as stationary for all practical purposes. Such time scales are:

a) the electrical relaxation time of the resistive electrodes on the order of milliseconds to seconds for common materials;
b) the electrical relaxation time of the medium resistivity layers (HV layers) and the drift time of the avalanche ions, on the scale of microseconds;
c) the development time of avalanches and streamers on the scale of nanoseconds.

Throughout the text time-average values will be denoted by bar. In principle all quantities are position dependent, except the obvious ones, such as applied voltages or when otherwise stated.

2. Some topics of RPC technology

The defining feature of RPC detectors is that always the volumes where gas amplification takes place are flat-shaped (“gas gaps”) and delimited by at least one resistive plate (resistive electrode). This plate limits the amount of charge that is instantaneously available to be transferred across the gap in case a spark develops, as no significative amount of charge can be conducted across the plate in the short time span of spark development. Such stunted sparks are, somewhat incorrectly, named “streamers” in RPC terminology.

Common resistive plate materials are phenolic-paper laminate[1] and glass. There is research on ceramic materials ([5], [6]) and low-resistivity glass [7] for high counting rate applications.

2.1. Arrangement of the electrodes

RPCs allow for a wide range of strategies for structure, high-voltage (HV) application and signal collection (pickup). The simplest scheme, depicted in Fig. 1, comprises just one metallic

[1] Commonly known as “bakelite”.

PoS(RPC2012)033

plate and one resistive electrode (RE) in electrical contact with a metallic foil or plate. HV can be applied on both electrodes, requiring HV resistors and coupling capacitors to the amplifier, or one side may be grounded, in which case the resistor and capacitor on that side may be omitted.

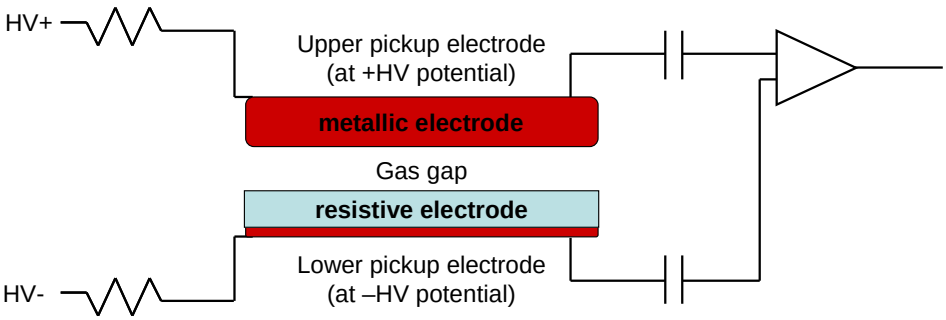

Fig. 1 – Illustration of the simplest RPC construction, featuring just a single gas gap defined by a resistive and a metallic electrode. If one electrode is to be grounded, then the corresponding resistor and capacitor may be omitted.

On the opposite extreme of complexity, the symmetric multigap construction allows to accumulate in a central pickup electrode the currents induced from many gas gaps. The multigap [10] construction introduces one or more electrically floating REs in between the galvanicaly connected ones, creating extra gas gaps without additional galvanic connections.

It is clear that many variations may be introduced along these general lines.

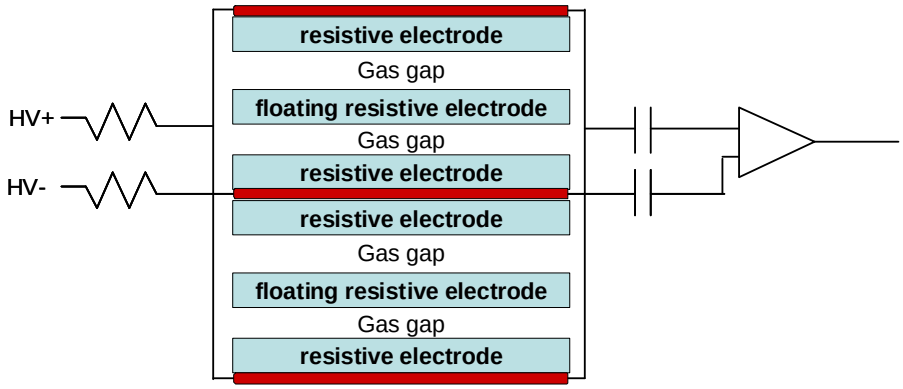

Fig. 2 – Illustration of the structure of the symmetric multigap construction. The electrically floating electrodes allow extra gas gaps to be created without additional electrical connections.

The metallic signal-pickup electrodes may be segmented in pads or strips, as needed for their effective readout.

2.2. Detector polarization

There are two basic methods for applying the HV to the REs, depicted in Fig. 3.

One possibility is to apply the HV to the same metallic electrode (ME) that collects the signal. This electrode must be in galvanic contact with the RE.

PoS(RPC2012)033

Another possibility is to apply HV to the RE via a medium-resistivity layer (RL) with much lower resistivity than the RE but much higher resistivity than the ME. The idea is that for the DC current (the "counting current") the voltage drop along the RL will be small compared with the drop in the RE, so for this purpose the RL can be considered as behaving as a good conductor, applying uniformly the HV to the RE and liberating the ME from this function. However, for the fast signals generated in the gas gap the RL will behave as an insulator, allowing the induced signal to be collected at the external MEs, which can be at any convenient DC potential. The non-ideal behaviour of the RL in either function must be taken into consideration in the modelling of the detector.

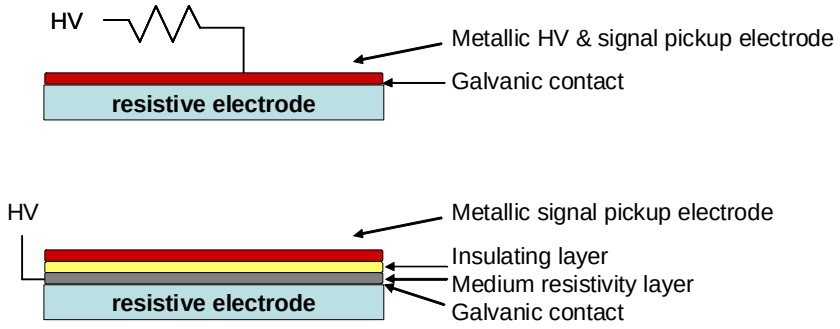

Fig. 3 – Depiction of the two principal methods to apply HV to the resistive electrodes. Top: direct galvanic contact with a metallic electrode that also collects the signal. Bottom: HV is applied to a layer of medium resistivity, which is in galvanic contact with the resistive electrodes.

3. Determination of the electric field in the gas gap

3.1. DC polarization

The current paths and voltage drops from the HV power supply and through the detector are approximately depicted in Fig. 4. In here we will consider the case of a multigap detector with HV applied via a RL as a representative case. The calculations can be easily adapted to other situations.

As far as the resistance of the RL will be much lower than the RE's the current lines will proceed inside the RL almost parallel to the plate and then cross the RE almost perpendicularly. An example of an exact numerical calculation is shown in Fig. 5.

In terms of DC polarization, that is, considering only the time-average values of the relevant quantities, we can state the following identities for each point on the chamber plane

$$\begin{aligned} \bar{V}_g &= \frac{V}{2} - \frac{3}{2}\bar{V}_{RE} - \bar{V}_{RL} \\ \bar{j} &= \bar{\phi}\bar{q} \\ \bar{V}_{RE} &= \rho d\, \bar{j} \end{aligned} \qquad (1)$$

PoS(RPC2012)033

where (all time-average quantities) $\bar{j}$ is the current density across the gas gap, $\bar{\phi}$ the inflow of particles crossing the detector, $\bar{q}$ the total charge generated per particle, V is the applied voltage. $\bar{V}_{RE}$ is the voltage drop across the RE, $\bar{V}_{RL}$ is the voltage drop along the RL, $\bar{V}_g$ is the gap voltage, d is the thickness of the RE and g is the thickness of the gas gap. The numerical factors are specific of the situation considered.

In these identities most quantities are position dependent, but largely independent point-to-point, as far as the voltage drops occur mostly perpendicular to the gas gap. The exception is V_{RL}, which depends on the details on how the RL is connected to the HV power supply, the current converging in such points.

In general a numerical calculation will be needed for V_{RL} but for simple situations useful analytical solutions can de derived. In the approximation of an infinitely long chamber in one direction, with the HV fed to the RL along the edges and a uniform average counting current $\bar{j}$, a simple calculation shows that

$$\bar{V}_{RL} = V - \Re \bar{j} \frac{x^2}{2} \tag{2}$$

being x is the distance from the edge and $\Re$ the surface resistance[1] of the RL. An example can be see in Fig. 5 b). Likewise, for a circular chamber fed along the rim

$$\bar{V}_{RL} = V - \Re \bar{j} \frac{r^2}{4} \tag{3}$$

where r is the distance from the rim. These two situations suggest that in general, for a chamber fed along the rim of the RL, V_{RL} will drop parabolically towards the centre, differing only the numerical factors in denominator.

For a rectangular chamber there is a Fourier series solution ([8] v.II pp.140)

$$\bar{V}_{RL} = V - \Re \bar{j} \sum_{n,m=0}^{\infty} C(n,m) \cos\left[(2n+1)\pi \frac{x}{a}\right] \cos\left[(2m+1)\pi \frac{y}{b}\right], \begin{cases} |x| < a/2 \\ |y| < b/2 \end{cases}$$
$$C = \frac{64(-1)^{n+m}}{\pi^4 (2n+1)(2m+1)\left(\frac{(2n+1)^2}{a^2} + \frac{(2m+1)^2}{b^2}\right)} \tag{4}$$

[1] The surface resistance of a thin layer of material is defined as the resistance that is measured between opposite sides of a square. This is independent of the size of the square and it is given by $\Re = \rho/h$, being ρ the resistivity of the material and h its thickness. Sometimes this quantity is named "resistance per square".

PoS(RPC2012)033

where *x* and *y* are the distances from the centre of the chamber, respectively along the sides with length *a* and *b*. It can be numerically verified that for a square chamber the voltage drop in the centre approaches (3) while for an elongated one it approaches (2).

Naturally the assumption of uniform $\bar{j}$ is not exact. Even if the incoming particle flow $\bar{\phi}$ is uniform, $\bar{q} = \bar{q}(V_g)$ and V_g that is itself a function of $\bar{j}$ via (1). In reality one needs a theory of $\bar{q}(V_g)$ (section 4.3) and a numerical calculation of $\bar{V}_{RL}(\bar{j}(x,y))$ to derive self-consistent local values for all quantities.

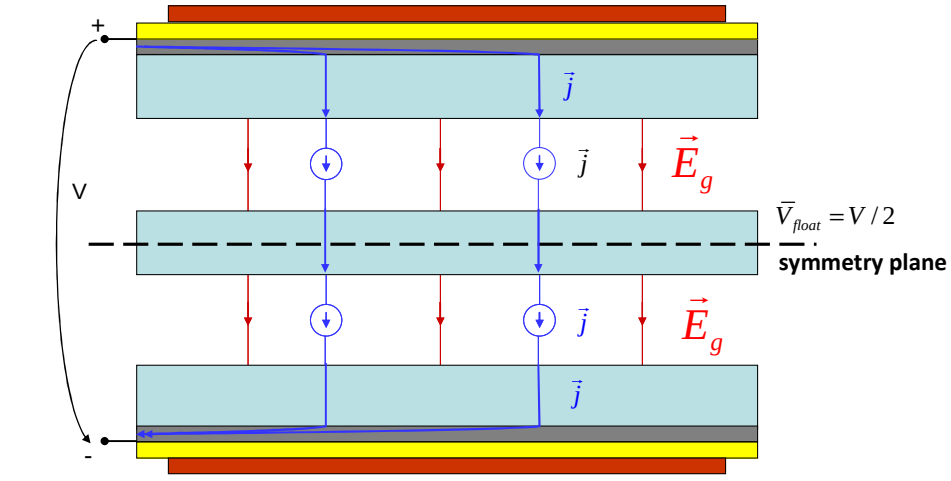

a)

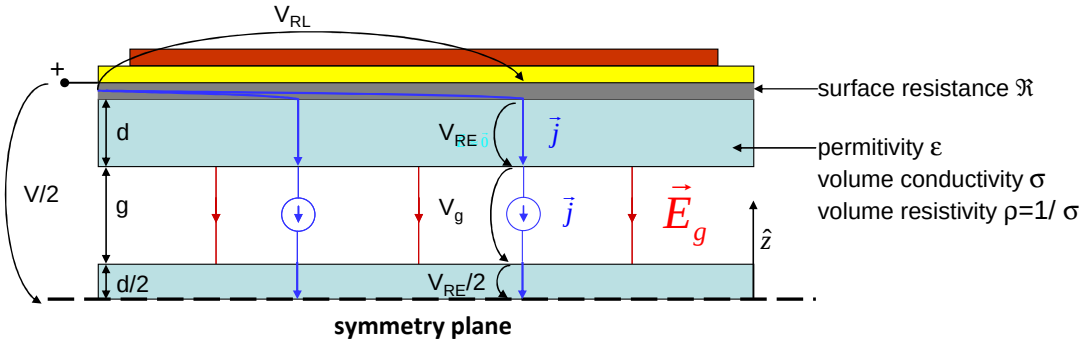

b)

Fig. 4 – a) Approximate representation of the current path across the detector, from the HV power supply poles. The current sources represent the current density created in the gas gap by the avalanches or other discharges that take place in there. An electric field $\vec{E}_g$ appears in the gas gap. Note that if the currents are the same in both gaps, by symmetry the average voltage in the centre of the floating RE must be $\bar{V}_{float} = V/2$. Legend: current lines – blue; electric field lines in the gas gap red; for other items see Fig. 3. b) Voltage drops across the several elements of an RPC, based on Fig. 4.

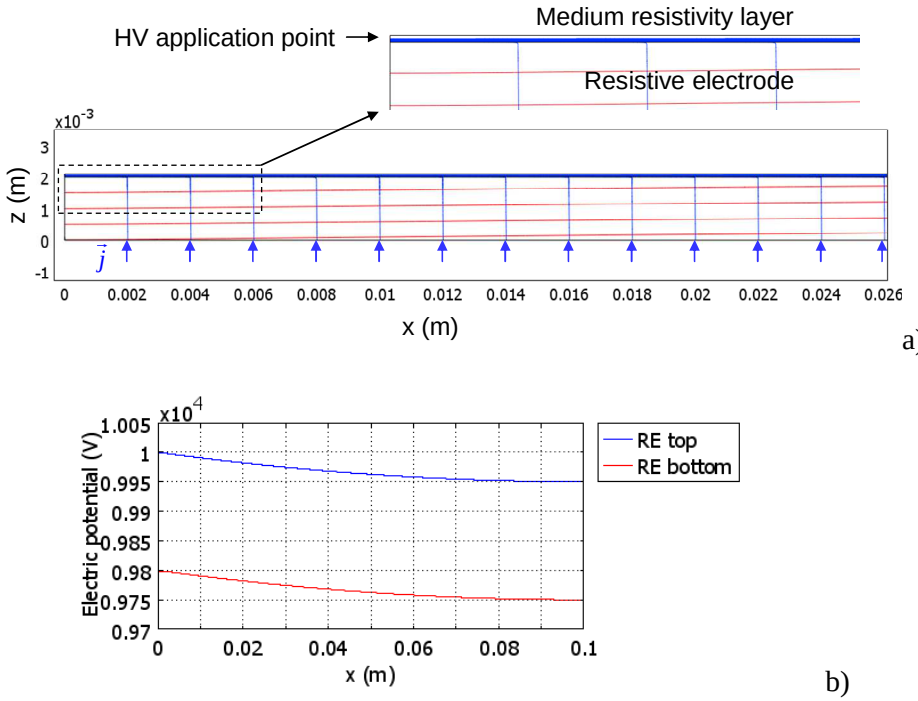

Fig. 5 – a) Example of a numerical calculation of the current and potential distribution on a cross-section of the RL-RE ensemble assuming translational symmetry perpendicular to the plane of the image. The HV contact is on the upper left face of the RL. Note that the isopotencial lines are not exactly parallel to the face of the RE. Parameters: RL surface resistance $\Re=10\ G\Omega$; RE resistivity $\rho=10^{13}\ \Omega\cdot cm$; injected current density $j=100\ pA/cm^2$. Legend: current lines – blue; isopotential lines in steps of 50 V – red. b) The electric potential along the top and bottom faces of the RE, showing a parabolic voltage drop of 50V between the edge and the center of the chamber (ΔV_1) and 200V across the RE (ΔV_2).

3.2. Fluctuations of the polarization

On top of the steady (time-average) aspects described above there will be fluctuations in time of the gap electric field

$$\vec{E}_g = \frac{V_g}{g}(-\hat{z}) \qquad (5)$$

owing to the field generated by the charges that the avalanches will deposit over the REs. A representation of this situation is shown in Fig. 6 for a simple RPC. As the perturbating electric field $\Delta\vec{E}_g$ also exists inside the RE there will be a collective motion of the conduction charges in there that will eventually cancel the deposited charge.

PoS(RPC2012)033

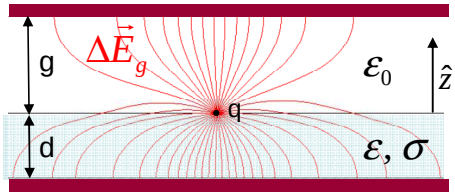

Fig. 6 – Representation of the electric field generated by a charge placed on the interface between the RE and the gas gap in a simple RPC.

The situation shown in Fig. 6 has been treated analytically [11], with the result for the perpendicular component of the perturbation field:

$$\Delta\vec{E}_g \cdot \hat{z} = \overbrace{\frac{q}{2\pi(\varepsilon+\varepsilon_0)} \frac{z e^{-t/\tau_1}}{\left(\rho^2+z^2\right)^{\frac{3}{2}}}}^{\text{infinitely thick layers}} + \overbrace{\frac{q}{2\pi} \int_0^\infty dk\, J_0(kr)\left(f_1(k,z) e^{-t/\tau(k)} - f_2(k,z) e^{-t/\tau_1} \right)}^{\text{contribution from the metallic electrodes}} \quad (6)$$

$$\tau_1 = \frac{\varepsilon+\varepsilon_0}{\sigma};\ \tau_2 = \frac{d\varepsilon}{g\sigma} + \frac{\varepsilon_0}{\sigma};\ \tau(k) \subset [\tau_1, \tau_2].$$

Most of the expression deals with the spatial variation (including the omitted f_1 and f_2) but the most interesting aspect is the time dependence. The perturbation field decays exponentially with a range of relaxation time constants bound by τ_1 and τ_2, as given in (6). For reasonable values of the physical parameters, taking glass as the RE material, these time constants will be of the order of seconds. In some circumstances it may not be unreasonable to take identical values for these parameters

$$\tau = \frac{d\varepsilon}{g\sigma} + \frac{\varepsilon_0}{\sigma} = \tau_2 \approx \tau_1 \quad (7)$$

in which case the time behaviour becomes analog to that of an RC circuit. (For equivalence with RC models τ_2 should be used.) In such RC models ([12], [13]) the space dependence is introduced as a box-like "effective perturbation area": avalanches falling onto this box charge an RC circuit that represents this area and have no action outside the box.

It is clear that in RPC structures more complex than shown in Fig. 6 the calculation of the perturbation will be more involved, eventually requiring a numerical approach. However the phenomenon will be physically similar and the present case can serve as a qualitative guide.

Having calculated the characteristics of each elementary perturbation one should address the problem of the collective perturbation arising from all avalanches depositing charge in the electrodes at random positions and times.

PoS(RPC2012)033

Naturally, a possibility is to proceed by Monte Carlo simulation, as shown in [11], Figure 2. Fluctuations of magnitude about ±1% of the applied field are visible superposed on an average field drop close to 8% for $\bar{\phi} = 600\,Hz/cm^2$.

A nimbler, however less accurate, way to proceed is to note that this is a "shot noise" process for which there is a simple theoretical result: Campbel's theorem. For the *rms* value of the instantaneous drop voltage across the RE this results in [13]

$$rms(V_{RE}) = \bar{V}_{RE}\sqrt{\frac{1+\left(\frac{rms(q)}{\bar{q}}\right)^2}{2\bar{N}}} \propto \sqrt{\bar{\phi}} \qquad (8)$$

$$\bar{N} = A\bar{\phi}\tau$$

which turns out to be proportional to the square root of the particle inflow. In here A is the "effective perturbation area" and $\bar{N}$ is the average number of avalanches that contribute to the perturbation. An estimate for the area A ($\tilde{A}$) can be determined from (6) [11] yielding $\tilde{A}=5.7mm^2$ for the case $g=0.3$ *mm* and $d=3$ *mm*.

At large values of $\bar{\phi}$ the dependence of $rms(q)/\bar{q}$ on V_g (to be discussed in section 5.3) must be included in (8) for good agreement with the corresponding MC simulation [13]. This actually reduces the fluctuations with respect to the unperturbed case.

It should be noted that in this section we were ignoring V_{RL}. The V_{RL} fluctuations haven't been treated in the literature, but, owing to the, in principle, much lower resistivity of the RL material, the time constants associated with the RL are certainly much smaller than the RE's.

3.3. Change of regime

When the RPC will go through a change of regime, for instance a sudden change of the particle inflow, there will be a transient imbalance of the DC polarization that will evolve in time with the time constant (7). For short bursts of radiation (compared with τ) this may simulate an effective lower resistivity of the RE [13].

4. Avalanches

Free "primary" electrons will appear in the gas gaps either by direct ionization of the gas by high-energy charged particles, creating electron-ion pairs, or by emission from the cathodes. The later can arise by photoelectric effect upon irradiation by ultraviolet photons, or presumably spontaneously, generating dark counts. No detailed study was made on the physical origin of dark counts in RPCs.

Each of the primary electrons will drift under the influence of the gap field $\vec{E}_g$ and eventually will gain enough energy to collision-ionize the gas molecules generating new electron positive-ion pairs. The new electrons thus freed will themselves undergo the same

PoS(RPC2012)033

process, generating a cascade process known as a Townsend avalanche. As the drift speed of the electrons is about a thousand times higher than that of the ions, these are left behind in a cloud that is essentially static in the time frame of the avalanche growth. These ions will eventually drift in the opposite direction but at the practical values of $\vec{E}_g$ never ionize themselves.

Many secondary processes can take place in avalanches (see e.g. [14]-[16] and references therein), the most relevant for RPCs being the formation of negative ions by electron capture if the gas mixture has any electronegative component. Indeed RPCs and PPCs[1] are the only gaseous detectors that can work in electronegative gas mixtures, which have a beneficial effect in their stable operation, even if not well understood.

As the electrons and ions drift, they go through random collisions that lead them astray of a straight path. If one considers a cloud of particles, such effect, called diffusion, causes the widening of the cloud.

4.1. Average avalanche growth (swarm model)

If one considers a large number of particles (a "swarm"), described by a particle density distribution, their collective behaviour can be described in detail by an hydrodynamic model (e.g.: [17]):

$$\begin{cases} a)\ \vec{\nabla}^2 V_{sc} = -\dfrac{\rho_{sc}}{\varepsilon_0} = -q_{p^+}\dfrac{n_{i+} - n_{i-} - n_e}{\varepsilon_0}\ \&\,\text{boundary conditions} \\ b)\ \vec{E} = -\vec{\nabla}V_{sc} + \vec{E}_g \\ c)\ \dfrac{\partial n_e}{\partial t} + \vec{\nabla}\cdot\vec{j}_e = S + (\alpha - \eta)\vec{j}_e\cdot\hat{W}_e\ \ \&\,\text{initial conditions} \\ d)\ \dfrac{\partial n_{i+}}{\partial t} + \vec{\nabla}\cdot\vec{j}_{i+} = S + \alpha\vec{j}_e\cdot\hat{W}_e \\ e)\ \dfrac{\partial n_{i-}}{\partial t} + \vec{\nabla}\cdot\vec{j}_{i-} = \eta\vec{j}_e\cdot\hat{W}_e \\ f)\ \vec{j}_a = \vec{W}_a n_a - D_a\vec{\nabla}n_a\Big|_{a=\{e,i+,i-\}} \end{cases} \tag{9}$$

where all quantities (to be described below) are time and position dependent.

In principle $\vec{E}_g(\vec{r},t)$ is the instantaneous applied field calculated from eqs. (1), (5), including eventual fluctuations. But it should be noted that the time scales involved in these are much longer than the phenomena here described and therefore $\vec{E}_g$ may well be considered as constant within the electron and ion transit time scale.

[1] Parallel-Plate Chamber: the fully metallic version of RPC.

PoS(RPC2012)033

Equation (9) a) is just Poisson's equation applied to the net space charge density (ρ_{sc}) created respectively by the electron, positive ion and negative ion numerical densities, $n_e(\vec{r},t)$, $n_{i+}(\vec{r},t)$, $n_{i-}(\vec{r},t)$. The elementary charge is $q_{p^+} = 1.60\times10^{-19} C$. Such equation must be accompanied by the relevant electrical boundary conditions, which must include the resistive materials. In most practical cases it is very likely that the relaxation times of those materials will be much longer than the very short time scale of avalanche development (few ns) and the resistive materials can be treated as pure dielectrics. In this case the avalanche calculations in RPCs are essentially similar to any other detector's.

Eq. (9) b) states that the total electric field $\vec{E}$ felt by the avalanche is the sum of the space-charge field and the applied field. If the former is comparable to the later the avalanche is said to be under the influence of the "space-charge effect", while if the former is much weaker than the later then $\vec{E} \approx \vec{E}_g$, (9) a) can be ignored and equations c) to e) become independent of each other. This is the "small avalanche", "proportional avalanche" or "Townsend avalanche" limit, so called because in average the total charge generated will be proportional to the amount of primary charge:

$$\begin{cases} \vec{E} = \vec{E}_g \\ \dfrac{\partial n_e}{\partial t} + \vec{\nabla}\cdot\vec{j}_e = S + (\alpha-\eta)\vec{j}_e\cdot\hat{W}_e \\ \dfrac{\partial n_{i+}}{\partial t} + \vec{\nabla}\cdot\vec{j}_{i+} = S + \alpha\vec{j}_e\cdot\hat{W}_e \\ \dfrac{\partial n_{i-}}{\partial t} + \vec{\nabla}\cdot\vec{j}_{i-} = \eta\vec{j}_e\cdot\hat{W}_e \\ \vec{j}_a = \vec{W}_a n_a - D_a\vec{\nabla}n_a\Big|_{a=\{e,i+,i-\}} \end{cases} \qquad \text{small avalanche limit} \qquad (10)$$

Equations (9) c) to e) are all similar and describe for each point in space what are the possible causes for a change in time of the densities of the different species (electron, positive ion, negative ion). These must be complemented with the relevant initial conditions.

The left hand side (lhs) of these eqs. is just the standard matter conservation equation, involving the total particle flow density for each species, given in (9) f). The parameter $\vec{W}_a$ is the respective swarm drift velocity, following the direction of $\vec{E}$ (or against for negative particles). The first term in the right hand side (rhs) of (9) f) is the drift particle flow density and the second term the diffusion particle flow density, also known as Fick's law. The parameter D_a is the diffusion coefficient.

PoS(RPC2012)033

The rhs of eqs. (9) c) to e) expresses particle creation or destruction. The factor $(\alpha-\eta)\left|\vec{W}_e\right|$ in (9) c) is the swarm net ionization rate (ionizations minus attachments per unit time)[1] and, multiplied by the electron flow density, accounts for the creation of new free electrons by ionization and for their destruction by attachment in electronegative mixtures, creating negative ions. The spatial rate of ionization is the "first Townsend coefficient" α (ionizations per unit electron swarm path) and the spatial rate of attachment is the attachment coefficient η (attachments per unit electron swarm path). For a given gas mixture, the magnitude of the parameters $\alpha,\eta,\vec{W}_a,D_a$ is a function of $\left|\vec{E}\right|$ only. The correspondence of these quantities on the remaining equations is straightforward, taking into attention the respective subscript labels.

The term *S* accounts for "other" sources of ionization, to be specified later.

Rigorously, the diffusion process is slightly different along the drift direction or along the direction perpendicular to it, originating slightly different diffusion coefficients in each of these directions. This fine point is generally disregarded in this type of calculations. Likewise, there is some dissent in the literature as whether the diffusion flow density should be included in the particle creation term. In here we have included such term, following [18], [19].

Owing to the very different electron and ion drift velocities a considerable simplification can be achieved with little error if one decouples the almost instantaneous creation of the ion cloud by the electron avalanche from its posterior slow drift and diffusion. Defining $\tilde{T}_e$ as the total progression time of the electron avalanche (must stop at the anode), (9) can then be simplified to

progression of the electron avalanche for $t < \tilde{T}_e$

$$\begin{cases} a)\ \vec{\nabla}^2 V_{sc} = -\dfrac{\rho_{sc}}{\varepsilon_0} = -q_{p^+}\dfrac{n_{i+,0}-n_{i-,0}-n_e}{\varepsilon_0}\ \&\ \text{boundary conditions} \\ b)\ \vec{E} = -\vec{\nabla}V_{sc} + \vec{E}_g \\ a)\dfrac{\partial n_e}{\partial t} + \vec{\nabla}\cdot\vec{j}_e = S + (\alpha-\eta)\vec{j}_e\cdot\hat{W}_e \\ b)\dfrac{\partial n_{i+,0}}{\partial t} = S + \alpha\vec{j}_e\cdot\hat{W}_e \\ c)\dfrac{\partial n_{i-,0}}{\partial t} = \eta\vec{j}_e\cdot\hat{W}_e \\ e)\ \vec{j}_e = \vec{W}_e n_e - D_e\vec{\nabla}n_e \end{cases} \qquad (11)$$

[1] In here the term "swarm" applied to a certain quantity implies that this is the local average of this quantity over the ensemble of all relevant particles that are present in this location. For instance, the swarm electron velocity at a point in space and time is the spatial average of the velocity of all electrons in the immediate vicinity of this point.

DISCUSS the connection between swarm approximation and real electrons.

PoS(RPC2012)033

ions' drift for t > $\tilde{T}_e$

$$\begin{cases} a)\ \vec{\nabla}^2 V_{sc} = -\dfrac{\rho_{sc}}{\varepsilon_0} = -q_{p^+}\dfrac{n_{i+} - n_{i-} - n_e(\tilde{T}_e)}{\varepsilon_0}\ \&\ \text{boundary conditions} \\ b)\ \vec{E} = -\vec{\nabla}V_{sc} + \vec{E}_g \\ c)\dfrac{\partial n_{i+}}{\partial t} + \vec{\nabla}\cdot\vec{j}_{i+} = 0,\ \text{ with } n_{i+}(\vec{r},0) = n_{i+,0}(\vec{r},\tilde{T}_e) \\ d)\dfrac{\partial n_{i-}}{\partial t} + \vec{\nabla}\cdot\vec{j}_{i-} = 0,\ \text{ with } n_{i-}(\vec{r},0) = n_{i-,0}(\vec{r},\tilde{T}_e) \\ e)\ \vec{j}_a = \vec{W}_a n_a - D_a\vec{\nabla}n_a\Big|_{a=\{i+,i-\}} \end{cases} \quad (12)$$

where $n_e(\tilde{T}_e)$ denotes the electron density after the progression of the electron avalanche, typically lying on the surface of the cathode. If the anode is metallic this is totally annulled by the image charge, but if the anode is resistive it will perturb the gap field, as discussed in section 3.2.

En rigueur, only in the diffusionless limit, when the avalanche is point-like, it is possible to define sharply the avalanche's progression time up to the anode. The progression time $\tilde{T}_e$ in (11) should be understood as a time at which the electron current becomes negligible, as it is never mathematically null (next section).

Is it worth noting that in this approximation and if *S* can be neglected, which is often the case, $n_{i+,0}$ and $n_{i-,0}$ are identically distributed in space and the net ion charge density $q_{p^+}(n_{i+} - n_{i-})$, which governs the space-charge effect, depends only on $(\alpha - \eta)$, likewise the electrons. Therefore only the combination $(\alpha - \eta)$ matters for the development of the avalanche.

4.2. Small avalanches

The small avalanche approximation was defined in (10) as the limit at which the electric field caused by the avalanches' own space-charge is negligible when compared to the applied field. In this limit considerable progress can be done analytically.

Very good expositions can be found in the literature; for instance Raether [26] gives all details on the case when diffusion is neglected. Much more complicated situations, involving detachment and metastable atoms are treated in [17], but this work focuses on a somewhat different point of view. As diffusion is a determinant process in RPCs, actually ruling the very important space-charge effect via the avalanche width, in here we will treat both the diffusionless and diffusive cases for an arbitrary point of release of a single primary electron-ion pair and the case of an uniform ionization line in the absence of diffusion. Other situations can be treated by superposition.

PoS(RPC2012)033

PROCEEDINGS OF SCIENCE

In this section we will use the geometry and quantities defined in Fig. 7. The avalanche starts at the origin of the (cylindrical) coordinates and progresses towards the anode at a distance z_0. The gap width is g.

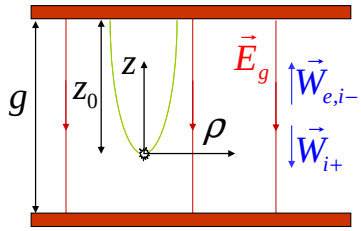

Fig. 7 – Definition of geometry, coordinate system and some quantities used in this section.

In the small avalanche limit the coefficients are constant and the equations (10) are linear. Taking additionally *S=0*, reasonably simple and useful solutions can be obtained. These conditions can be somewhat relaxed at the expense of more opaque expressions [27].

From the linearity of the equations it follows that the evolution of an arbitrary initial distribution $n_a(\vec{r},0)$ can be calculated by convolution:

$$n_a(\vec{r},t) = \int_{\text{all space}} n_a(\vec{r}',0)\,\underset{\sim}{n}_a(\vec{r}-\vec{r}',t)\,d\vec{r}' \Big|_{a=\{e,i\pm\}} . \tag{13}$$

where $\underset{\sim}{n}_a(\vec{r},t)$ is the impulse response for each relevant species and for each initial electron-ion pair position $\vec{r}$. Owing to the presence of the electrodes, the impulse response is dependent on the position the initial electron.

Combining (10) and (11) one gets:

$$\begin{cases} a)\ \dfrac{\partial \underset{\sim}{n}_e}{\partial t} + \vec{\nabla}\cdot\vec{\underset{\sim}{j}}_e = \alpha^*\,\vec{\underset{\sim}{j}}_e\cdot\hat{W}_e \\ b)\ \dfrac{\partial \underset{\sim}{n}_{i+,0}}{\partial t} = \alpha\,\vec{\underset{\sim}{j}}_e\cdot\hat{W}_e \\ c)\ \dfrac{\partial \underset{\sim}{n}_{i-,0}}{\partial t} = \eta\,\vec{\underset{\sim}{j}}_e\cdot\hat{W}_e \end{cases} \quad \textbf{progression of the electron avalanche} \quad \text{for } t < \tilde{T}_e$$

$$\begin{cases} d)\ \dfrac{\partial \underset{\sim}{n}_{i\pm}}{\partial t} + \vec{\nabla}\cdot\vec{\underset{\sim}{j}}_{i\pm} = 0, \ \text{for } t > \tilde{T}_e, \text{ with } \underset{\sim}{n}_{i\pm}(\vec{r},0) = \underset{\sim}{n}_{i\pm,0}(\vec{r},\tilde{T}_e) \quad \textbf{ions' drift} \\ e)\ \vec{\underset{\sim}{j}}_a = \vec{W}_a\underset{\sim}{n}_a - D_a\vec{\nabla}\underset{\sim}{n}_a\Big|_{a=\{e,i\pm\}} \end{cases} \tag{14}$$

where, for compactness, we will use $(\alpha-\eta)=\alpha^*$. The main equation to be solved is (14) a). Once $\underset{\sim}{n}_e$ is known it is simple to calculate the ion densities

PoS(RPC2012)033

$$\underset{\sim}{n}_{i\pm,0}(t)=\begin{pmatrix}\alpha\\ \eta\end{pmatrix}\int_0^t \underset{\sim}{\vec{j}}_e(t')\cdot\hat{W}_{i\pm}\,dt'+\begin{pmatrix}1\\ 0\end{pmatrix}\delta(z) \tag{15}$$

where for $\underset{\sim}{n}_{i+,0}$ we added an extra ion at the origin, the pair of the initial electron. Taking into account the presence of the anode, the positive and negative ions distribution generated by the electron avalanche and that will flow later to the, respectively, cathode and anode are

$$\underset{\sim}{n}_{i\pm}(\vec{r},0)=\underset{\sim}{n}_{i\pm,0}(t=\tilde{T}_e) \tag{16}$$

The flow of ions to the electrodes is calculated by the convolution (13) of (16) with the impulse solution of (14) d), $\underset{\sim}{h}_{i\pm}$, which is a particular case of the solution of (14) a):

$$\underset{\sim}{n}_{i\pm}(\vec{r},t)=\int_{all\ space}\underset{\sim}{n}_{i\pm}(\vec{r}',0)\,\underset{\sim}{h}_{i\pm}(\vec{r}-\vec{r}',t)\,d\vec{r}' \tag{17}$$

The total number of generated ions is

$$\underset{\sim}{N}_{i\pm}=\int_{gap}\underset{\sim}{n}_{i\pm}(\vec{r},0)\,dV=\int_{z0-g}^{z_0}\int_0^{\infty}\underset{\sim}{n}_{i\pm}(\vec{r},0)\,2\pi\rho\,d\rho\,dz \tag{18}$$

which should agree with the total flow of particles through the electrode planes

$$\begin{aligned}\underset{\sim}{N}_a&=\int_0^{\infty}\underset{\sim}{j}_{a,z}(z_0,t)\,dt\\ \underset{\sim}{N}_{i+}&=\int_0^{\infty}\underset{\sim}{j}_{i+,z}(z_0-g,t)\,dt\end{aligned}\Bigg|_{a=\{e,i-\}} \tag{19}$$

where $j_{a,z}$ is the total particle flow in the z direction:

$$\underset{\sim}{j}_{a,z}=\int_0^{\infty}\underset{\sim}{\vec{j}}_a\cdot\hat{W}_a\,2\pi\rho\,d\rho\Big|_{a=\{e,i\pm\}}$$

The currents and total charges induced in the external electrodes by the different particles will be

$$\begin{aligned}\underset{\sim}{I}_{a(ind)}&=\gamma\int_{gap}\underset{\sim}{\vec{j}}_a\cdot\hat{W}_a\,dV=\gamma\int_{z_0-g}^{z_0}\underset{\sim}{j}_{a,z}\,dz\\ \underset{\sim}{Q}_{a(ind)}&=\int_0^{\infty}\underset{\sim}{I}_{a(ind)}\,dt\end{aligned}\Bigg|_{a=\{e,i\pm\}} \tag{20}$$

PoS(RPC2012)033

where γ is an electrical induction factor with units of charge per length defined in section 6.1, (96), (97)[1].

4.2.1. Diffusionless limit

Very simple and useful expressions can be derived for the case when diffusion can be neglected ($D_a = 0$ in (14) e)). In this case the diffusionless solution of (14) a) is

$$\underset{\sim}{n}_e = \mathrm{e}^{\alpha^* W_e t}\delta\left(z - W_e t\right) \tag{21}$$

where $\delta(x)$ is Dirac's delta function. This represents a point-like avalanche that progresses in the gap with velocity W_e along z, containing at $t = 0$ a single electron at $z = 0$. Therefore, the radial coordinate is not necessary and it was omitted. The vanishing of the avalanche when it encounters the anode at $z = z_0$ is not part of this solution and must be taken into account externally.

Of course, in the diffusionless limit the particle flow density is only in the z direction and given by

$$\underset{\sim}{j}_a = \underset{\sim}{j}_{a,z} = W_a \underset{\sim}{n}_a\Big|_{a=\{e,i\pm\}} \tag{22}$$

The number of electrons in the avalanche is (19):

$$\underset{\sim}{N}_e = \mathrm{e}^{\alpha^* z_0} \tag{23}$$

which, in the diffusionless limit, is equal to the total avalanche charge when it touches the anode: $\int_{gap} \underset{\sim}{n}_e(t = z_0 / W_e)\, dV = \mathrm{e}^{\alpha^* z_0}$.

Following (20), the current and charge induced by the electrons is

$$\underset{\sim}{I}_{e(ind)} = \gamma W_e \mathrm{e}^{\left(\alpha^* W_e t\right)}\theta\left(z_0 - W_e t\right) \tag{24}$$

$$\underset{\sim}{Q}_{e(ind)} = \gamma \frac{\mathrm{e}^{\alpha^* z_0} - 1}{\alpha^*} = \gamma \underset{\sim}{N}_{e(ind)} \tag{25}$$

where $\theta(x) = \int_{-\infty}^{x} \delta(x')\, dx'$ is the Heaviside function and we have defined the quantity $\underset{\sim}{N}_{e(ind)}$ (number of created electrons/α^*) for later use.

The ion distributions created in the gap by the progressing electron avalanche are, following (15)

[1] For metallic anode and cathode $\gamma = q_{p^+} / g$

PoS(RPC2012)033

$$\underset{\sim}{n}_{i\pm,0}(t)=\begin{pmatrix}\alpha\\ \eta\end{pmatrix}\mathrm{e}^{\alpha^* z}\left[\theta(z)-\theta(W_e t-z)\right]+\begin{pmatrix}1\\ 0\end{pmatrix}\delta(z) \tag{26}$$

which results (16) in the ion distribution at $t=\tilde{T}_e=z_0/W_e$

$$\underset{\sim}{n}_{i\pm}(\vec{r},0)=\begin{pmatrix}\alpha\\ \eta\end{pmatrix}\mathrm{e}^{\alpha^* z}\left[\theta(z)-\theta(z-z_0)\right]+\begin{pmatrix}1\\ 0\end{pmatrix}\delta(z) \tag{27}$$

and the corresponding total number of generated ions is (18)

$$\underset{\sim}{N}_{i\pm}=\begin{pmatrix}\alpha\\ \eta\end{pmatrix}\underset{\sim}{N}_{e(ind)}+\begin{pmatrix}1\\ 0\end{pmatrix} \tag{28}$$

The number of generated particles (including the primary pair) of each species respect the properties (the first being an obvious necessity)

$$\begin{aligned}&\underset{\sim}{N}_{i+}-\underset{\sim}{N}_{e}-\underset{\sim}{N}_{i-}=0\\ &\underset{\sim}{N}_{tot}=\underset{\sim}{N}_{i+}+\underset{\sim}{N}_{e}+\underset{\sim}{N}_{i-}=2\left(\alpha\underset{\sim}{N}_{e(ind)}+1\right)\end{aligned} \tag{29}$$

Note that in the absence of attachment ($\eta=0$) the second line reduces to $\underset{\sim}{N}_{tot}=2\underset{\sim}{N}_{e}$, which is a necessary property as well.

The impulse solutions of (14) d) are, respectively

$$h_{i\pm}=\delta(z-W_{i\pm}t) \tag{30}$$

which upon convolution (13) with (27) yield the drifting ion charge densities

$$\underset{\sim}{n}_{i\pm}=\begin{pmatrix}\alpha\\ \eta\end{pmatrix}e^{\alpha^*(z+W_{i\pm}t)}\left[\theta(z-W_{i\pm}t)-\theta(z-z_0-W_{i\pm}t)\right]+\begin{pmatrix}1\\ 0\end{pmatrix}\delta(z+W_{i\pm}t) \tag{31}$$

which is are just clipped drifting exponentials. (Note that $W_{i+}<0$, $W_{i-}>0$.) The presence of the electrodes is not contained in this solution.

Defining the ionic particle flow densities as in (22) it can be verified that (18) agrees with (19).

Applying (20), the induced current densities are

$$\begin{aligned}\underset{\sim}{I}_{i+(ind)}&=\gamma W_{i+}\left[1+\frac{\alpha}{\alpha^*}\left(\mathrm{e}^{\alpha^* z_0}-1\right)\right.\\ &\left.-\left(1+\frac{\alpha}{\alpha^*}\left(e^{\alpha^*(z_0-g+W_{i+}t)}-1\right)\right)\theta\left(z_0-g+W_{i+}t\right)\right]\theta\left(g-W_{i+}t\right)\\ \underset{\sim}{I}_{i-(ind)}&=\gamma W_{i-}\frac{\eta}{\alpha^*}\left(\mathrm{e}^{\alpha^*(z_0-W_{i-}t)}-1\right)\theta\left(z_0-W_{i-}t\right)\end{aligned} \tag{32}$$

PoS(RPC2012)033

A representation of these currents can be seen in Fig. 8.

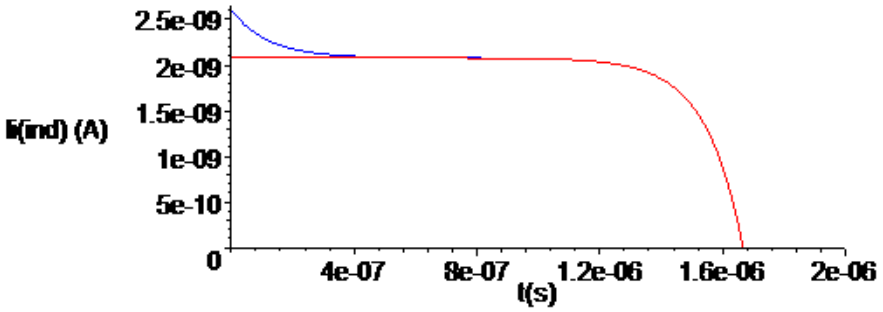

Fig. 8 – Representation of the positive ions current and the total ionic current in the diffusionless case for parameters $\alpha = 40\ mm^{-1}$, $\eta = 10\ mm^{-1}$, $W_e = 130\ mm/\mu s$, $W_{i\pm} = 0.3\ mm/\mu s$, $z_0 = 0.35\ mm$, $g = 0.5\ mm$, $\gamma = q_{p^+}/g$. All subsequent figures of this section will be represented with these parameters.

Substituting $z_0 = g = d$ in (32) one recovers eqs. 2.25 and 2.26 of [26].

The ionic induced charges are (20)

$$\begin{aligned} Q_{i+(ind)} &= \gamma\left[\frac{\alpha}{\alpha^*}\left(\left(\alpha^* g - 1\right)N_{e(ind)} + z_0\right) + g - z_0\right] \\ Q_{i-(ind)} &= \gamma\frac{\eta}{\alpha^*}\left(N_{e(ind)} - z_0\right) \end{aligned} \tag{33}$$

The total induced charge can be written as

$$\begin{aligned} Q_{(ind)} &= Q_{e(ind)} + Q_{i+(ind)} + Q_{i-(ind)} = \gamma g\frac{N_{tot}}{2} \\ &= \gamma g + \alpha g Q_{e(ind)} \end{aligned} \tag{34}$$

The first line expresses the necessary property that the total induced charge is proportional to half of the total number of generated particles (twice the number of electrons), just reflecting the fact that particles are produced in pairs and that the full drift of each pair induces the charge equivalent to a single elementary charge. The second line is specific of Townsend multiplication: for large gas gains the electronic (fast) induced charge is a fixed fraction of the total induced charge: $Q_{(ind)}/Q_{e(ind)} \approx \alpha g$. Note that for a chamber delimited by metallic electrodes (a PPC) $\gamma g = q_{p^+}$.

The expressions presented so far are for a single primary electron-ion pair: the impulse solution. Other situations can be calculated by superposition, on account of the linearity of the

PoS(RPC2012)033

base equations. As an example we will calculate a uniform ionization across the gap, totalling one electron-ion pair. In this case any impulse quantity $\underset{\sim}{X}(z_0)$ will correspond to

$$X(z_0)=\frac{1}{g}\int_0^g \underset{\sim}{X}(z_0)\,dz_0 \tag{35}$$

The result for the induced currents is

$$\begin{aligned} I_{e(ind)} &= \gamma W_e \frac{g-W_e t}{g} e^{\alpha^* W_e t}\theta(g-W_e t) \\ I_{i+(ind)} &= \frac{\gamma W_{i+}}{\alpha^* g}\left[\frac{\alpha}{\alpha^*}\left(e^{\alpha^* g}-e^{\alpha^* W_{i+}t}\right)-\eta(g-W_{i+}t)\right]\theta(g-W_{i+}t) \\ I_{i+(ind)} &= \frac{\gamma W_{i-}\eta}{\alpha^* g}\left[\frac{e^{\alpha^*(g-W_{i-}t)}}{\alpha^*}-(g-W_{i-}t)-1\right]\theta(g-W_{i-}t) \end{aligned} \tag{36}$$

reproducing eqs. 2.31 and 2.35 of [26], while there is a slight discrepancy on 2.34. A representation of the currents' development can be seen in Fig. 9, along with a comparison with (24) and (32).

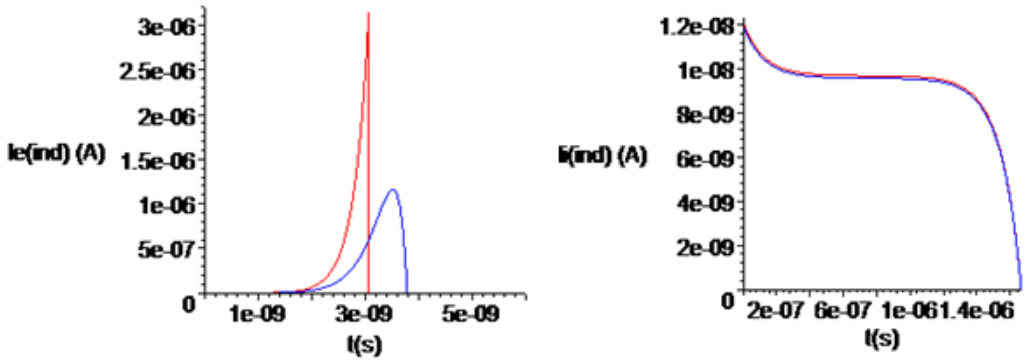

Fig. 9 – Representation of the induced electronic (left) and total ionic (right) currents for uniform ionization across the gap and for a single electron avalanche starting at $z_0=\ln\left((e^{\alpha^* g}-1)/(\alpha^* g)\right)/\alpha^*$ which results in the same total amount of electronic induced charge. While the electronic currents are quite different in shape, the ionic currents are undistinguishable.

The corresponding induced charges are

PoS(RPC2012)033

$$Q_{e(ind)} = \gamma \frac{e^{\alpha^* g} - \alpha^* g - 1}{\alpha^{*2} g} = \gamma N_{e(ind)}$$
$$Q_{i+(ind)} = \gamma \left[\alpha \left(g - \frac{1}{\alpha^*} \right) N_{e(ind)} + \left(\frac{\alpha}{\alpha^*} + 1 \right) \frac{g}{2} \right] \quad (37)$$
$$Q_{i-(ind)} = \gamma \frac{\eta}{\alpha^*} \left(N_{e(ind)} - \frac{1}{2} g \right)$$

It is clear that relations that don't depend explicitly on z_0, such as (29) and (34), are not changed by the distribution of the primary charges and remain true.

Comparison between (37) and (24), (33) shows that at high gas gain the ratio between the induced charge (electronic or ionic) generated from a single electron released from the cathode and the induced charge generated from the same amount of primary charge distributed evenly across the gap approaches $\alpha^* g$.

4.2.2. Drift and diffusion

1.1.1.1 Electrons

We start by noticing that the function

$$\underset{\sim}{n}_e(\vec{r},t) = \exp\left(\alpha^* W_e t\right) \frac{\exp\left(-\frac{\rho^2}{4D_e t}\right)}{4\pi D_e t} \frac{\exp\left(-\frac{(z-vt)^2}{4D_e t}\right)}{\sqrt{4\pi D_e t}} \quad (38)$$
$$v = W_e + \alpha^* D_e$$

is a solution of the electron's equation (14) a) [19] and that $\lim_{t\to 0} \underset{\sim}{n}_e = \delta(\vec{r})$, $\delta(\vec{r})$ being the tridimensional Dirac delta function. That is, $\underset{\sim}{n}_e$ describes the electronic particle density of an elementary avalanche issuing from a single electron at the origin. The total number of particles contained in the avalanche grows exponentially in time as $\exp\left(\alpha^* W_e t\right)$, moves with velocity $v = W_e + \alpha^* D_e$ and spreads gaussianly with variance $2D_e t$ (so $FWHM = 2.36\sqrt{2D_e t}$). Essentially this is what is shown in Fig. 15 a) for the proportional region *t<3 ns*, as the initial width was made extremely small. Note that the swarm electron velocity v is slightly larger than the average electrons physical velocity W_e. This is possible because v denotes the movement of a mathematical point (the point of highest swarm density), which is not bound by physical constraints.

Similar impulse responses apply to eqs. (14) d), with the obvious exchange of labelling and setting $\alpha^* = 0$.

Often we will need (38) integrated over the plane parallel to the electrodes:

PoS(RPC2012)033

$$\underset{\sim}{n}_e(z,t)=\int_0^\infty \underset{\sim}{n}_e(\rho,z,t)2\pi\rho\, d\rho=\exp\left(\alpha^* W_e t\right)\frac{\exp\left(-\frac{(z-v_e t)^2}{4D_e t}\right)}{\sqrt{4\pi D_e t}} \tag{39}$$

The electrons' flow density is in this case given by (14) e),

$$\vec{\underset{\sim}{j}}_e=\underset{\sim}{n}_e(\vec{r},t)\frac{\rho\hat{e}_\rho+(z+(W_e-\alpha^* D_e)t)\hat{e}_z}{2t}=\underset{\sim}{n}_e(\vec{r},t)\vec{\underset{\sim}{v}}_e(\vec{r},t) \tag{40}$$

where $\hat{e}_\rho,\hat{e}_z$ are the unit vectors in the direction of each coordinate axis and $\vec{\underset{\sim}{v}}_e(\vec{r},t)$ is the local velocity of the electron swarm. (Not to be confused with the constant v defined above – $\vec{\underset{\sim}{v}}_e(\vec{r},t)$ results from the usual definition of flow density $\vec{j}=n\vec{v}$.) The total flow in the z direction (integrated radially) is

$$\underset{\sim}{j}_{e,z}=\underset{\sim}{n}_e(z,t)\frac{z+(W_e-\alpha^* D_e)t}{2t}=\underset{\sim}{n}_e(z,t)\underset{\sim}{v}_e(z,t) \tag{41}$$

where $v_e(z,t)=\vec{\underset{\sim}{v}}_e(\vec{r},t)\cdot\hat{e}_z$ is the swarm velocity in the z direction.

Note that for negative z, particularly in the first instants of the avalanche, when the density gradients are stronger, there can be a flow of electrons towards the cathode ($j_{e,z}<0$) in some regions of the avalanche. Under the formulation of the hydrodynamic model (9) these negative flows will generate "negative particles" that are obviously unphysical. In here these are integrated in, so there is an implicit, although slight, approximation.

The total number of electrons $\underset{\sim}{N}_e$ generated by the elementary avalanche (38) is, following (19):

$$\underset{\sim}{N}_e=e^{\alpha^* z_0} \tag{42}$$

In this aspect there is no difference between this one and the diffusionless case discussed in the previous section.

Following (20) and making the slight approximation of disregarding the presence of the cathode ($g=\infty$), the electronic induced current and charge is given by

$$\underset{\sim}{I}_{e(ind)}=\frac{1}{2}\gamma\exp\left(\alpha^* W_e t\right)\left[W_e\left(1+\operatorname{erf}\left(\frac{z_0-vt}{2\sqrt{D_e t}}\right)\right)-\sqrt{\frac{D_e}{\pi t}}\exp\left(-\frac{(z_0-vt)^2}{4D_e t}\right)\right] \tag{43}$$

$$\underset{\sim}{Q}_{e(ind)}=\gamma\frac{\underset{\sim}{N}_e-1}{\alpha^*}=\gamma\underset{\sim}{N}_{e(ind)} \tag{44}$$

PoS(RPC2012)033

It is quite remarkable that the calculation yields a total electronic induced charge that is the same as in the diffusionless case (24). A representation of both (24) and (43) is shown in Fig. 10.

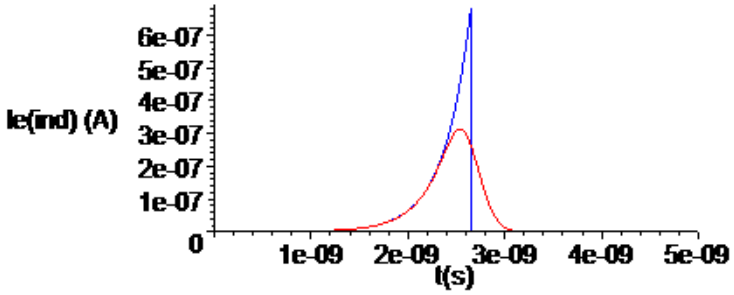

Fig. 10 – Electronic induced current with and without diffusion ($D_e \to 0$) calculated for the same parameters as in Fig. 15 and $D_e = 7.08\times10^{-2}\ mm^2/\mu s$. The corresponding induced charge is the same for both cases..

Concerning the treatment of other initial distributions, for instance, if the initial electron distribution is Gaussian with variance σ^2 , centred in the origin and containing N_0 electrons, it results from (13) and (38):

$$n_e(\vec{r},0) = N_0 \frac{\exp\left(-\frac{\rho^2+z^2}{2\sigma^2}\right)}{(2\pi\sigma^2)^{3/2}}$$
$$n_e(\vec{r},t) = N_0 \exp\left(\alpha^* W_e t\right) \frac{\exp\left(-\frac{\rho^2+(z-v_e t)^2}{2\left(2D_e t+\sigma^2\right)}\right)}{\left(2\pi(2D_e t+\sigma^2)\right)^{3/2}} \qquad (45)$$

which is gaussian with variance equal to the sum of variance of the initial distribution with the variance resulting from diffusion.

1.1.1.2 Ions

The ion distribution generated during the avalanche follows (15), which explicitly becomes

$$\underset{\sim}{n}_{i\pm,0}(\vec{r},t) = \begin{pmatrix}\alpha\\ \eta\end{pmatrix} \int_0^t \underset{\sim}{n}_e(\vec{r},t') \frac{z+(W_e-\alpha^* D_e)t'}{2t'} dt' + \begin{pmatrix}1\\ 0\end{pmatrix}\delta(z) \qquad (46)$$

Apart from the initial electron-ion pair, both distributions follow the same spatial-temporal development and differ only by the relative factor α/η . This integral cannot be evaluated

PoS(RPC2012)033

analytically. A numerical example is presented in Fig. 11, illustrating the fact that the correct superimposition of the electron and ion distributions, fundamental for the space-charge effect, depends on the correct modelling of diffusion

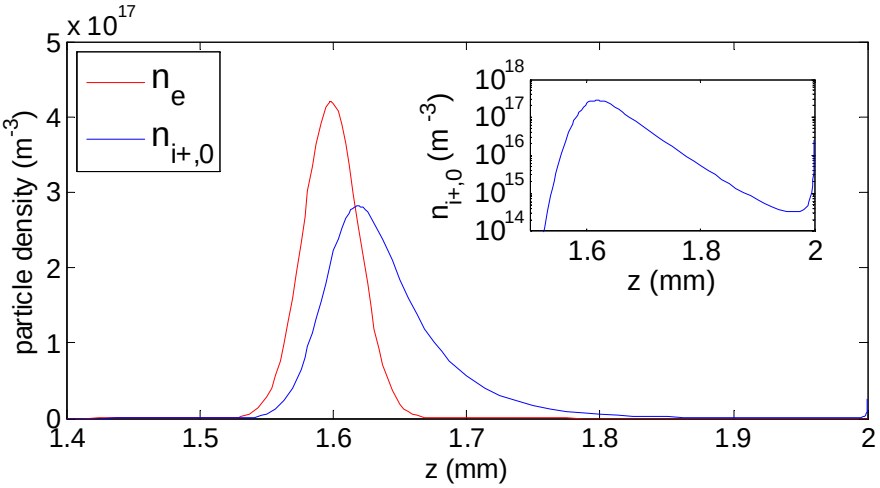

Fig. 11 – Electron and net (positive-negative) ion density calculated according to (38) and (46) (numerically) along the central line of the avalanche ($\rho=0$) for the parameters of Fig. 15, $t=3$ *ns*. As in this picture the avalanche proceeds from right to left it can be directly compared with Fig. 15. The inset shows that the ion density over the central line has a relatively limited range, as diffusion spreads the charge as the avalanche proceeds.

In the diffusive case the electron avalanche progression time $\tilde{T}_e$ must be taken mathematically as infinite (in practice only a few electron transit times) because (38) is never mathematically null for finite time. The ion distributions remaining in the gas gap after the avalanche is over are

$$\underset{\sim}{n}_{i\pm}(\vec{r},0)=\begin{pmatrix}\alpha\\ \eta\end{pmatrix} f\left[\theta(z)-\theta(z-z_0)\right]+\begin{pmatrix}1\\ 0\end{pmatrix}\delta(\vec{r})$$

$$f=\frac{1}{8u\pi r}\left[(1-u)\alpha^*+\left((1-u)\alpha^*+2\frac{u}{r}\right)\frac{z}{r}\right]\exp\left(\frac{1}{2}\frac{\alpha^*}{u}\left(r(u-1)+z(1+u)\right)\right) \qquad (47)$$

$$u=\alpha^* D_e / W_e;\quad r=\sqrt{\rho^2+z^2}$$

whose z profile after radial integration is just

$$\underset{\sim}{n}_{i\pm}(z,0)=\begin{pmatrix}\alpha\\ \eta\end{pmatrix}\mathrm{e}^{\alpha^* z}\left[\theta(z)-\theta(z-z_0)\right]+\begin{pmatrix}1\\ 0\end{pmatrix}\delta(z) \qquad (48)$$

and the corresponding total number of generated ions is

$$\underset{\sim}{N}_{i\pm}=\begin{pmatrix}\alpha\\ \eta\end{pmatrix}\underset{\sim}{N}_{e(ind)}+\begin{pmatrix}1\\ 0\end{pmatrix} \qquad (49)$$

PoS(RPC2012)033

exactly the same as in the diffusionless case. Note that although the electron swarm (38) has a Gaussian radial profile the ions' (47) hasn't.

The impulse solutions of (14) d) are the travelling and expanding Gaussians:

$$h_{i\pm}(\vec{r},t)=\frac{\exp\left(-\frac{\rho^2}{4D_{i\pm}t}\right)}{4\pi D_{i\pm}t}\frac{\exp\left(-\frac{\left(z-W_{i\pm}t\right)^2}{4D_{i\pm}t}\right)}{\sqrt{4\pi D_{i\pm}t}} \tag{50}$$

$$h_{i\pm}(z,t)=\int_0^\infty h_{i\pm}(\vec{r},t)\,2\pi\rho\,d\rho=\frac{\exp\left(-\frac{\left(z-W_{i\pm}t\right)^2}{4D_{i\pm}t}\right)}{\sqrt{4\pi D_{i\pm}t}} \tag{51}$$

To calculate the distribution of drifting ions one should convolve (47) with (50) over all space, which can be done only numerically. In Appendix I it is justified that, owing to the Gaussian radial profile of both (40) and (50), if in the end we are interested only in the longitudinal distributions (integrated radially) one may instead convolve only the longitudinal distributions (48) and (51), yielding

$$\begin{aligned} n_{i\pm}(z,t)=&\frac{1}{2}\begin{pmatrix}\alpha\\ \eta\end{pmatrix}\exp\left(az+b\right)\left[\operatorname{erf}\left(\frac{z+d}{c}\right)-\operatorname{erf}\left(\frac{z+e}{c}\right)\right]+\\ &\begin{pmatrix}1\\ 0\end{pmatrix}\frac{\exp\left(-\frac{\left(z-W_{i\pm}t\right)^2}{c^2}\right)}{\sqrt{\pi}c}\\ a=\alpha^*,&\quad b=\alpha^*\left(\alpha^* D_{i\pm}-W_{i\pm}\right)t,\quad c=2\sqrt{\left(D_{i\pm}t\right)}\\ d=\left(2\alpha^* D_{i\pm}-W_{i\pm}\right)t,&\quad e=d-z_0 \end{aligned} \tag{52}$$

The corresponding ion flow density is given by

PoS(RPC2012)033

$$\underset{\sim}{j}_{i\pm}(z,t)=\frac{1}{2}\binom{\alpha}{\eta}\Bigg[\left(W_{i\pm}-D_{i\pm}a\right)\left(\operatorname{erf}\left(\frac{z+d}{c}\right)-\operatorname{erf}\left(\frac{z+e}{c}\right)\right)$$
$$-2D_{i\pm}\frac{\exp\left(-\frac{(z+d)^2}{c^2}\right)-\exp\left(-\frac{(z+e)^2}{c^2}\right)}{\sqrt{\pi}c}\Bigg]\exp\left(a\,z+b\right)$$
$$+\binom{1}{0}\frac{\left(W_{i\pm}c^2+2D_{i\pm}\left(z-W_{i\pm}t\right)\right)\exp\left(-\frac{(z-W_{i\pm}t)^2}{c^2}\right)}{\sqrt{\pi}c^3} \tag{53}$$

of which a representation is shown in Fig. 12. Note that the presence of the electrodes is not part of this solution.

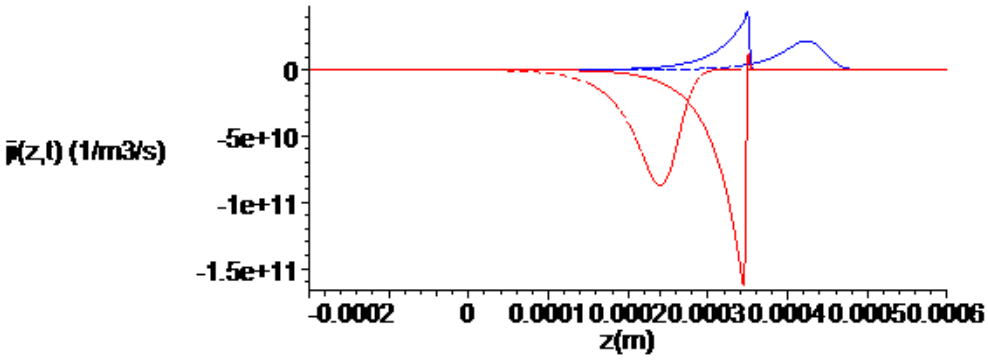

Fig. 12 – Representation of the positive (red lines) and negative (blue lines) ion densities for t=0 ns (solid lines) and t=300 ns (dashed lines). The positive ions count as negative flow, as the positive z direction lies towards the anode. Note that the electrodes are not incorporated in these solutions, so the swarms flow indefinitely.

The induced ion currents are

PoS(RPC2012)033

$$
\begin{aligned}
I_{i\pm(ind)} &= \gamma W_{i\pm}\Big[\big(f_{\pm}(z_0,a,b,c,d)-f_{\pm}(z_0-g,a,b,c,d)\big)\\
&\quad -\big(f_{\pm}(z_0,a,b,c,e)-f_{\pm}(z_0-g,a,b,c,e)\big)\\
&\quad +\frac{1}{2}\binom{1}{0}\left(\operatorname{erf}\left(\frac{-z_0+g+W_{i\pm}t}{c}\right)-\operatorname{erf}\left(\frac{-z_0+W_{i\pm}t}{c}\right)\right)\Big]\\
&\quad -D_{i\pm}\left[n_{i\pm}(z_0,t)-n_{i\pm}(z_0-g,t)\right]
\end{aligned}
\tag{54}
$$

$$
\begin{aligned}
f_{\pm}(x,a,b,c,d) &= \binom{\alpha}{\eta}\frac{1}{2a}\Big[\exp(a\,x+b)\operatorname{erf}\left(\frac{x+d}{c}\right)+\\
&\quad +\exp\left(b+\frac{1}{4}a^2c^2-ad\right)\operatorname{erf}\left(\frac{1}{2}ac-\frac{x+d}{c}\right)\Big]
\end{aligned}
$$

of which a representation is shown in Fig. 13

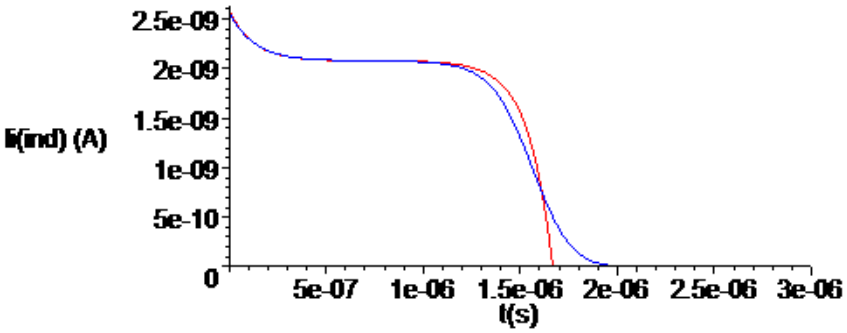

Fig. 13 – Representation of the total ionic currents with and without diffusion. The same charge is induced in both cases. $D_{i\pm} = 5.0\times10^{-4}\ mm^2/\mu s$.

Remarkably, the ionic induced charges calculated after (20) and (54) are exactly the same as for the diffusionless case (33), equally holding the properties (34).

4.2.3. Space-charge field

Neglecting the presence of the electrodes (close to a spatially small avalanche distant from the electrodes) the space-charge field can be approximately calculated for the small avalanche approximation. However, when the field becomes significative relatively to the applied field the small avalanche approximation ceases to be valid.

It is clear that the point-like avalanche approximation presented in section 4.2.1 doesn't produce any realistic field, so only the diffusive case can be considered.

Owing to its spherical symmetry, the field created by the electronic part of a small avalanche (38) can be straightforwardly calculated by application of Gauss' law of electrostatics, yielding

PoS(RPC2012)033

$$\vec{E}_e = -\frac{q_{p^+} e^{\alpha^* W_e t}}{4\pi\varepsilon_0 r^2}\left(\operatorname{erf}\left(\frac{r}{2\sqrt{D_e t}}\right) - r\frac{\exp\left(\frac{-r^2}{4D_e t}\right)}{\sqrt{\pi D_e t}}\right)\left(\frac{\rho}{r}\hat{e}_\rho + \frac{z-vt}{r}\hat{e}_z\right) \qquad (55)$$

$$r = \sqrt{\rho^2 + (z-vt)^2}$$

pointing towards the centre of the electron cloud at $\rho = 0,\ z = vt$. Naturally, superimposition will apply. This is however limited to the electron swarm under the small avalanche limit. As soon as there will be some space-charge effect the electron distribution loses its spherical symmetry and (55) will become inaccurate. The ion's distribution (46) is not spherically symmetric in any case.

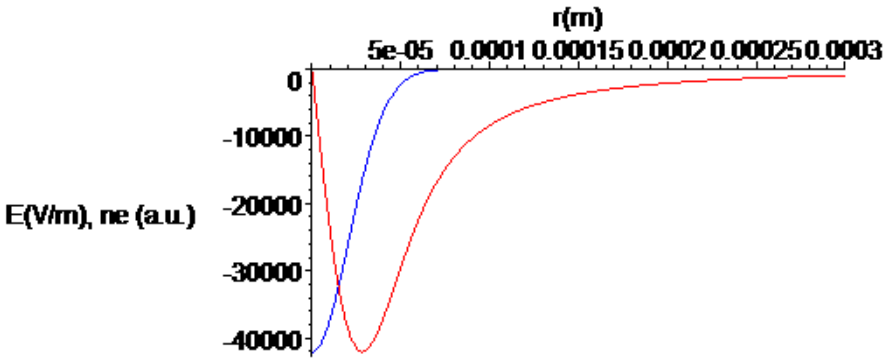

Fig. 14 – Representation of the radial electric field (55) generated by the electron swarm (red line). For comparison, the electron charge density (38) is represented in blue.

It is more general to consider only rotational symmetry, which is preserved in any case of the swarm approximation. A ring of radius a centred at the origin and containing the constant linear charge density λ creates the potential and field ([8] v.I pp. 176)

$$V(\rho,z,a) = \frac{\lambda a}{\pi\varepsilon_0}\frac{K(k)}{r_1}$$

$$\vec{E}(\rho,z,a) = \frac{\lambda a}{\pi\varepsilon_0}\left[\frac{1}{2r_1\rho}\left(K(k) - \frac{\left(a^2-\rho^2+z^2\right)E(k)}{r_1^2\left(1-k^2\right)}\right)\hat{e}_\rho + \frac{z\,E(k)}{r_1^3\left(1-k^2\right)}\hat{e}_z\right] \qquad (56)$$

$$k = \frac{2\sqrt{a\rho}}{r_1},\quad r_1 = \sqrt{(a+\rho)^2+z^2}$$

PoS(RPC2012)033

where $K(k)$ and $E(k)$ are the complete elliptic integrals of the first and second kinds. Over the axis (56) simplifies to a well known result

$$V(0,z,a)=\frac{\lambda}{2\varepsilon_0}\frac{1}{\sqrt{(z/a)^2+1}}$$
$$\vec{E}(0,z,a)=\frac{\lambda}{2\varepsilon_0}\frac{a\,z}{\left(z^2+a^2\right)^{3/2}}\hat{e}_z \tag{57}$$

For a rotationally symmetric volume charge distribution $h(\rho,z)$ the superposition formula will be just the convolution

$$V_h(\rho,z)=\iint_{All\ space} h(\rho',z')\frac{V(\rho,z-z',\rho')}{\lambda}d\rho'dz' \tag{58}$$

with a similar formula for the field.

In particular, for a radially Gaussian volume charge distribution $h=\lambda(z,t)\,e^{-\rho^2/\left(2\sigma^2(t)\right)}/\left(2\pi\sigma^2(t)\right)$, such as the integrand of (46), the radial contribution to the axial field can be integrated analytically

$$E_h(0,z,t)=\int_{-\infty}^{\infty}\lambda(z',t)u(z-z',t)dz'$$
$$u(z,t)=\frac{1}{4\varepsilon_0}\left(\frac{\left(\operatorname{erf}\left(\frac{1}{2}\frac{|z|\sqrt{2}}{\sigma(t)}\right)-1\right)\exp\left(\frac{1}{2}\frac{z^2}{\sigma^2(t)}\right)z}{\sqrt{2\pi}\sigma^3(t)}+\frac{z}{\pi\sigma^2(t)|z|}\right) \tag{59}$$

The remainder of the calculation must be performed numerically.

4.3. Space-charge effect

The space-charge field causes two effects: reduction of the avalanche gain because for the bulk of the swarm the electric field is reduced with respect to the applied field and promotion of the appearance of runaway self-sustained discharges called “streamers”. The former effect is observable in a number of ways (see, for instance, [26] section 3.7, [28], [29]):

- for fixed irradiation and geometry the growth of the induced charge with the applied voltage deviates from the exponential behaviour (25) and becomes almost linear;
- the ratio of electronic to total induced charge become larger than the ratio given in (34) for Townsend avalanches;

PoS(RPC2012)033

- the charge spectrum changes its shape, with suppression of the larger avalanches.

4.3.1. Numerical calculations

An example of a calculation of the electron avalanche performed by finite elements for an axially symmetric avalanche is shown in Fig. 15. The gas (pure tetrafluorethane) parameters were taken from [20] and the applied field is $E_g = 60\,kV/cm$. Attachment is small in this gas and it was ignored. The *S* term was also taken to be zero.

A tiny electron swarm containing the charge of one electron is started very close to the cathode with a Gaussian spatial density distribution and then drifts downwards while multiplying and growing in size by diffusion. An ion cloud trails behind, with partial superimposition. For development times up to 3 ns the velocity is constant and the shape of the electron's isodensity lines is circular, while after this time there is an apparent acceleration and distortion of the electron swarm owing to the space-charge effect. This can be verified in Fig. 15 b) top left panel, which shows that up to 3 ns the electric field is essentially equal to the applied field, while for 5 ns there is a quite strong distortion. At this time most of the ion swarm is under the influence of a reduced electric field (the electrons are "pushed back" by the positive ions) and it can be seen (same figure, rhs panel) that the initial exponential current growth is thwarted. This self-control of the avalanche charge via the space-charge effect is a fundamental feature of the avalanche-mode RPC operation (e.g. [21]-[25]).

It is clear that the full 3D solution of (11) requires extremely heavy numerical machinery.

Naturally, avalanches can as well be modelled by pure microscopic Monte-Carlo methods, following all details of the movement of every particle. However, for large avalanches containing up to 10^8 charged particles this is hardly a practical proposition.

An interesting combination of both methods is the method of "clouds", where small parts of the avalanche are propagated over a short time step following the analytical solutions for small avalanches subject to the local electric field. The field is then recalculated after each step and the process re-iterated. One advantage of this method is that the avalanche gain fluctuations can be incorporated in the propagation of the sub-avalanches. It was successfully applied to the calculation of axially symmetric avalanches [24].

PoS(RPC2012)033

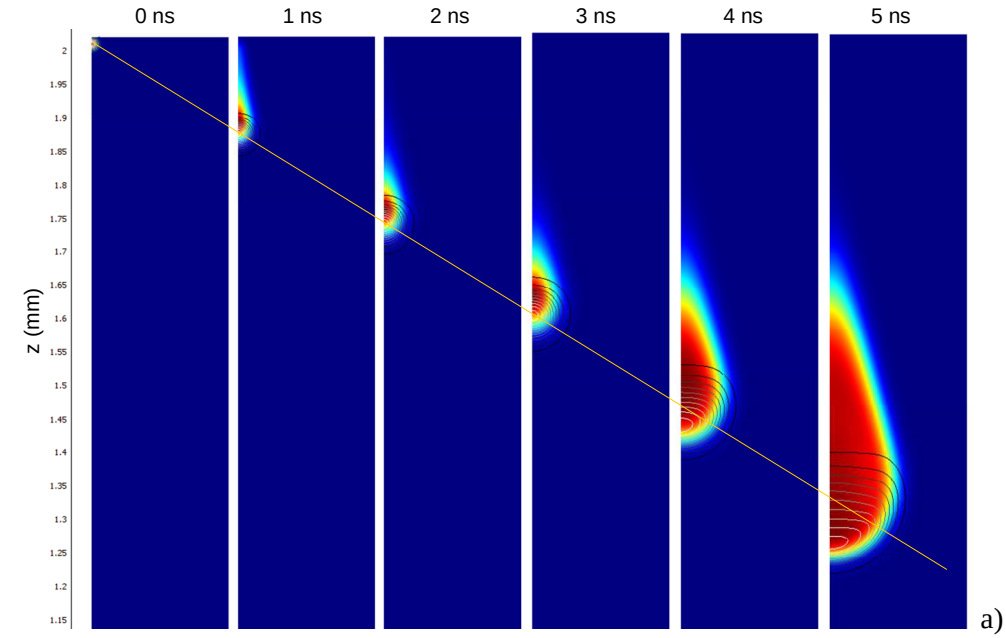

a)

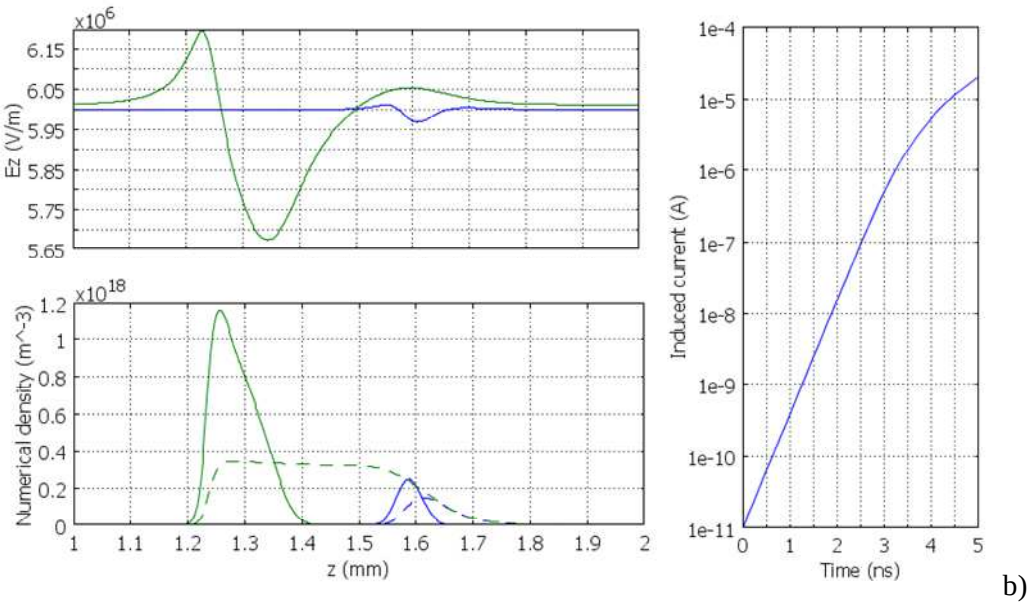

b)

Fig. 15 - Representation of the development of an axially symmetric avalanche following the hydrodynamic approach, (11). a) Cross-section of the charge distributions around the symmetry axis. The gray contour lines represent the percentiles of the electron distribution (isodensity lines) while the colour map represents the percentiles of the density of ions. The yellow line represents the electron's drift velocity. The avalanche was started from the cathode (z=2 mm). Note that for times up to 3ns the velocity is constant and the shape of the electron's isodensity lines is invariable, while after this time there is an apparent acceleration and distortion of the swarm. b) – Top left panel: electric field along the centre of the avalanche after 3ns (blue line) and 5 ns (green line). Bottom left panel: corresponding electron (solid line) and ion (dashed line) numerical densities. Right panel: induced current, showing the initial exponential growth and the onset of space-charge effect after 3 ns.

PoS(RPC2012)033

4.3.2. Analytical models

Besides numerical calculations, there were attempts to parameterize the space-charge effect in some compact formula that might reproduce the experimental data, typically modifying (14) a) by the introduction of a charge-dependent effective first Townsend coefficient $\alpha_{eff} = \alpha_{eff}\left(N_e\right)$.

Before going into details we need to formulate (14) a) in simplified way. Neglecting diffusion the avalanche is point-like (21). Inserting already α_{eff}, volume integration (18) of both members of (14) a) yields

$$\frac{dN_e(t)}{dt} = \alpha_{eff} W_e N_e(t) \qquad t < z_0 / W_e \tag{60}$$

Of course, at $t = z_0 / W_e$ the avalanche reaches the anode and stops. This equation may be restated in terms of the avalanche progression length as

$$\frac{dN_e(z)}{dz} = \alpha_{eff} N_e(z) \qquad z < z_0 \tag{61}$$

Neglecting attachment, the total induced charge will be, after (29) and (34), just $Q_{(ind)} = \breve{Q}_{e(ind)} + \breve{Q}_{i+(ind)} = \gamma g N_e$, while $\breve{Q}_{e(ind)}$ and $\breve{Q}_{i+(ind)}$ depend on the specific space-charge models.

In the following, $N_{e,sat}$ denotes the indicative charge scale at which the transition from the Townsend to the space-charge regime occurs.

Raether's formulation ([26] section 3.7) is

$$\begin{aligned} \alpha_{eff} &= \alpha && N_e \le N_{e,sat} \\ \alpha_{eff} &= \alpha\left(1 - B\ln\left(N_e / N_{e,sat}\right)\right) && N_e > N_{e,sat} \end{aligned} \tag{62}$$

It is apparent that the multiplication ceases if $B\ln\left(N_e / N_{e,sat}\right) = 1$, so the solution converges to the asymptotic value $N_{e,max} = N_{e,sat}\mathrm{e}^{1/B}$. The solution is

$$\begin{aligned} N_e &= N_0 e^{\alpha z} && z \le z_{sat} = \ln\left(N_{e,sat} / N_0\right) / \alpha \\ N_e &= N_{e,sat} \exp\left[\frac{1 - \mathrm{e}^{-B\alpha(z - z_{sat})}}{B}\right] && z > z_{sat} \end{aligned} \tag{63}$$

The two segments match to the first derivative.

Aielli's formulation [28] amounts to

PoS(RPC2012)033

$$\alpha_{eff} = \alpha\left(1 - N_e / N_{e,sat}\right) \tag{64}$$

and the solution of (61) is then integrated to yield

$$N_e = N_0 + N_{e,sat} \ln\left(\frac{1+e^{\alpha(z-z_0)}}{1+e^{-\alpha z_0}}\right) \tag{65}$$

where z_0 is a free parameter. The asymptotic behaviour is linear: $N_e \underset{N_e \gg N_{e,sat}}{\simeq} N_{e,sat}\alpha z + cte$.

The formulation of [22], which is here slightly expanded, is

$$\alpha_{eff} = \frac{\alpha}{1+\left(N_e / N_{e,sat}\right)^m} \tag{66}$$

with the solution

$$N_e = N_{e,sat} \sqrt[m]{w\left(K\, \mathrm{e}^{M+m\alpha z}\right)},\ K = \left(N_0 / N_{e,sat}\right)^m \tag{67}$$

where $w(x)$ is Lambert's function [30] defined by $e^{w(x)}w(x) = x$. The asymptotic behaviour is $N_e \underset{N_e \gg N_{e,sat}}{\simeq} N_{e,sat}\sqrt[m]{m\alpha z} + cte$, linear for $m = 1$ as approximately observed experimentally.

A comparison between the more exact numerical approach and the analytical ones is still missing.

4.4. Avalanche fluctuations

The avalanche growth is not fully deterministic, particularly on the initial stages of the avalanche when the number of electrons is lower than about one hundred (see for instance [31] Figure 6). After this stage the avalanche growth proceeds deterministically, essentially as described in sections 4.2 and 4.3. As a result, the final avalanche charge and the other related quantities will fluctuate around the average values given in these sections. As we will need later to consider other sources of fluctuations, will label this as the stochastic process $\mathcal{A}$.

As the stochastic behaviour is concentrated in the very first stages of the avalanche, when the avalanche charge is small, it is useful to describe the stochastic variations as a fictious random initial charge $\mathcal{N}_0$ with probability distribution function (PDF) $P_{\mathcal{A}}\left(\mathcal{N}_0\right)$ and unit average value that will then multiply deterministically according to a deterministic function $\mathcal{N}_e(\mathcal{N}_0)$, reaching a final average value $\mathcal{N}_e$. In these conditions the PDF of $\mathcal{N}_e$ is given by [25]

PoS(RPC2012)033

$$P_{\mathcal{A}}\left(\mathcal{N}_e\right) = P_{\mathcal{A}}\left(\mathcal{N}_0\right)\Big|_{\mathcal{N}_0=\mathcal{N}_0(\mathcal{N}_e)} \left|\frac{\partial \mathcal{N}_0}{\partial \mathcal{N}_e}\right| \tag{68}$$

where $\mathcal{N}_0(\mathcal{N}_e)$ is the inverse function of $\mathcal{N}_e(\mathcal{N}_0)$. Naturally, all these functions and PDFs are also function of other problem variables, such as α, d, z_0, etc. These concepts are illustrated in Fig. 16.

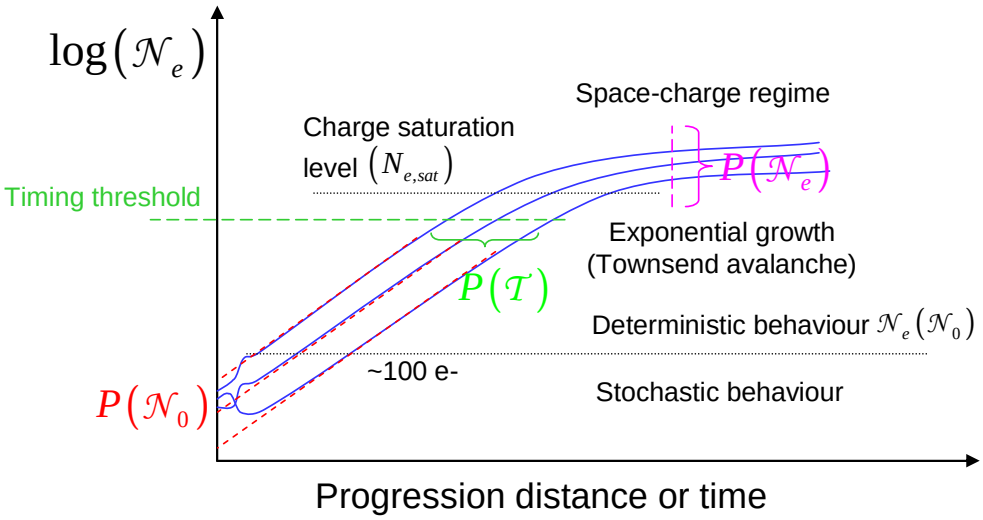

Fig. 16 – Illustration of the concepts subjacent to (68). The avalanche charge $\mathcal{N}_e(z)$ (blue line) has initially an erratic (stochastic) behaviour until it reaches a level of about 100 electrons. Then the behaviour is largely deterministic, starting by an exponential growth region (small avalanche). At some charge $(N_{e,sat})$ the space-charge regime sets in and there is a departure from exponential growth. The stochastic part can be taken into consideration by exponential back-extrapolation from the exponential growth region (red lines), generating the fictious distribution $P(\mathcal{N}_0)$, which is deterministically propagated in time via the function $\mathcal{N}_e(\mathcal{N}_0)$. If charge is measured after a certain development length it will be visible the charge distribution $P(\mathcal{N}_e)$. If the development time is measured at a certain charge threshold level, it will be produced the time distribution $P(\mathcal{T})$.

It seems to be a reasonable approximation [25] to use for $\mathcal{N}_e(\mathcal{N}_0)$ average relations of the kind (63). However, the need to calculate the derivative in (68) restricts its use to models on which the large-charge behaviour depends on $\mathcal{N}_0$. Of the models described in section 4.3 only (67) satisfies this property. However in [25] these models were modified in order to allow their use in this context [32] and it was found that all of them described similarly the available data.

PoS(RPC2012)033

4.4.1. Small avalanches

For the calculation of $P_{\mathcal{A}}(\mathcal{N}_0)$ one may consider the stochastic evolution of a small avalanche, progressing by a distance z, which is generally accepted as being given by Legler's avalanche theory. For sufficiently large $\mathcal{N}_e$ (approx. $\mathcal{N}_e \geq 100$) the Laplace transform of $P_{\mathcal{A}}(\mathcal{N}_e)$, $M_{\mathcal{A}}(\mathcal{N}_e)$, also called the moment-generating function (MGF), is given by [33]

$$M_{\mathcal{A}}(s) = \frac{N_e(1-r)s + r}{N_e s + r},\ r = 1 - \frac{\eta}{\alpha},\ N_e = e^{\alpha^* z} \tag{69}$$

where s is the complex frequency. Laplace-transform inversion yields

$$P_{\mathcal{A}}(\mathcal{N}_e) = (1-r)\delta(\mathcal{N}_e) + r\frac{r}{N_e}e^{-\mathcal{N}_e r/N_e} \tag{70}$$

This is actually a mixture of two distributions. A δ distribution at zero charge with weight $1-r$, corresponding to the probability that the avalanche will be extinguished owing to the electronegativity of the gas represented by η, and, with weight r, an exponential distribution with average value N_e / r. Therefore the average value of $P_{\mathcal{A}}(\mathcal{N}_e)$ is N_e.

If the avalanche is started by m electrons the corresponding PDF is the m-fold self-convolution of (70), with MGF $\left(M_{\mathcal{N}_e}\right)^m$. The explicit PDF is given in [33], [34]. In [33] it is also discussed the exact case.

Considering that for a small avalanche the swarm charge is proportional to $\mathcal{N}_0$, $\mathcal{N}_e(\mathcal{N}_0) = \mathcal{N}_0 e^{\alpha^* z} = \mathcal{N}_0 N_e$, it can be easily seen from (68) and (70) that

$$P_{\mathcal{A}}(\mathcal{N}_0) = (1-r)\delta(\mathcal{N}_0) + r^2\,\mathrm{e}^{-\mathcal{N}_0 r} \tag{71}$$

4.4.2. Large avalanches (space-charge regime)

In here we will touch the case of fixed-length avalanches, which is theoretically interesting but seldom realized in RPCs, as the ionizing particles will leave an ionization trail. The only circumstances where this may be realized is the amplification of the dark noise, presumably (but hasn't been investigated) generated by single electrons emitted by the cathode, or a dedicated experiment [25].

As stated above, the avalanche gain distribution $P_{\mathcal{A}}(\mathcal{N}_e)$ under influence of space-charge effect may be calculated from (68) and (71) by application of a $\mathcal{N}_e(\mathcal{N}_0)$ function, for which it can be used the space-charge model (67) (or any other for which the derivative $d\mathcal{N}_0 / d\mathcal{N}_e$ is

PoS(RPC2012)033

meaningful, that is, $\mathcal{N}_e$ actually depends on $\mathcal{N}_0$ in a non-trivial way). The necessary model functions are

$$N_0\left(N_e\right) = N_{e,sat}\sqrt[m]{w\left(K'\mathrm{e}^{K'-m\alpha z}\right)}, \quad K' = \left(N_e / N_{e,sat}\right)^m$$
$$\left|\frac{\partial N_0}{\partial N_e}\right| = \frac{1+K'}{\sqrt[m]{K'}}\frac{\sqrt[m]{w\left(K'\mathrm{e}^{K'-m\alpha z}\right)}}{1+w\left(K'\mathrm{e}^{K'-m\alpha z}\right)} \tag{72}$$

An example of the $P_{\mathcal{A}}\left(\mathcal{N}_e\right)$ thus obtained is shown in Fig. 17, to be compared with the data in [25] Figure 1.

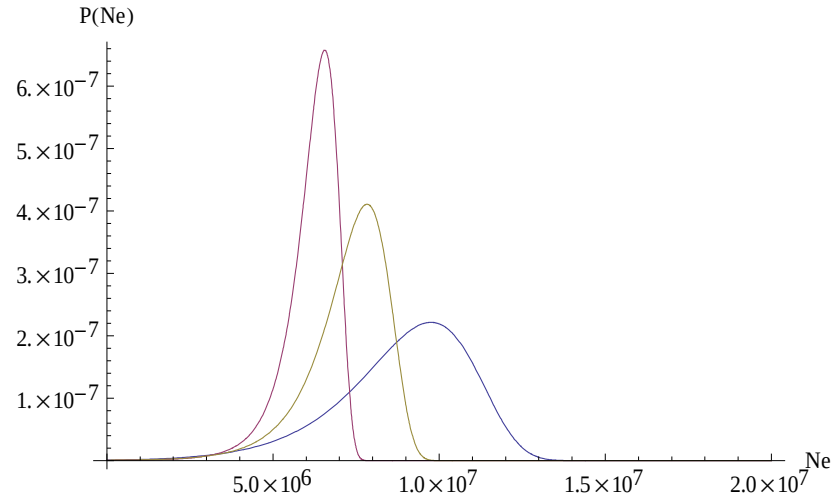

Fig. 17 – Representation of $P_{\mathcal{A}}\left(\mathcal{N}_e\right)$ calculated from (68), (71) and (72) for $\alpha = 70\,mm^{-1}$, $N_{e,sat} = 2\times10^6$, $z = 0.3\,mm$, $m = \{1, 1.5, 2\}$. The parameters $N_{e,sat}$ and m control the large charge behaviour.

5. Signal fluctuations

Even if the detector is irradiated with perfectly identical particles, the signal generated will not be equal for each particle. Apart from the avalanche gain fluctuations described in section 4.4 (process $\mathcal{A}$), there are other sources of fluctuations contributing to the final generated charge: the cluster statistics (process $\mathcal{B}$), the position z_0 of each cluster (process $\mathcal{C}$) and the variable number of clusters generated by each particle (process $\mathcal{D}$).

Secondary, technological, factors are the polarization fluctuations treated in section 3, either stochastic or position-dependent, and geometric variations, most importantly gap-width variations, which can be treated in the framework of a small-perturbations approach.

PoS(RPC2012)033

The coherent combination of all these fluctuations hasn't been treated theoretically. However, solutions for some particular cases of importance are known. Naturally, numerical calculations by Monte Carlo are possible [31], [22].

5.1. Primary ionization

As high-energy charged particles cross the RPC gas gap, ionization clusters will be produced in the gas. Such clusters originate from collisions with the atomic electrons, ionizing the atom. The ejected electron may produce further local ionization producing an ionization cluster. The ensemble of the electrons produced by a passing ionizing particle is called "primary charge". An illustration is shown in Fig. 18.

The number n of clusters (process $\mathcal{D}$) is Poisson-distributed with PDF and generating function, respectively,

$$P_{\mathcal{D}}(n) = \frac{\mathrm{e}^{-\lambda d}(\lambda g)^n}{n!}$$
$$C_{\mathcal{D}}(\zeta) = \mathrm{e}^{\lambda d(\zeta-1)} \qquad (73)$$

where λ is the average cluster density and therefore λg is the average number of clusters produced in the gas gap.

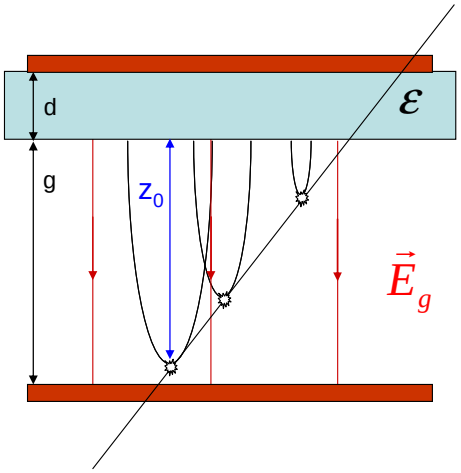

Fig. 18 – Representation of the ionization process in RPCs. The crossing charged particles deposit a random number of charge clusters at random locations. Each cluster contains a variable number of electron-ion pairs.

The details of the primary charge production are better simulated by tools such as HEED [35]. For minimum-ionizing particles the amount of pairs in a cluster (process $\mathcal{B}$) obeys approximately the empirical statistic

$$P(n_0) \propto n_0^{-2} \qquad (74)$$

PoS(RPC2012)033

In here this contribution will be not taken into account, but a comprehensive treatment of its influence on the time resolution, along with many statistical techniques useful in this context, is given in [33].

5.2. Time distribution

The time distribution $P(\mathcal{T})$ obtained by measuring the avalanche development time corresponding to a certain threshold induced current and avalanche charge $I_{e(ind),th} = \gamma W_e N_{e,th}$ (in the spirit of (24)), as illustrated in Fig. 16, has been calculated by several authors ([34], [36]) culminating in a very comprehensive treatment by Riegler [33]. In here it will be presented only a streamlined and slightly simplified calculation (neglecting process $\mathcal{B}$) and the main results.

In the spirit of (68), the change of variable relevant for the determination of time will be

$$P(\mathcal{T}) = P(\mathcal{N}_0)\Big|_{\mathcal{N}_0=\mathcal{N}_0(\mathcal{T})} \left|\frac{\partial \mathcal{N}_0}{\partial \mathcal{T}}\right| \tag{75}$$

for which we need to know the function $\mathcal{T}(\mathcal{N}_0)$ and its inverse. Note that we are calculating the intrinsic time jitter of the detector, neglecting any external factor, such as electronics. Experience seems to indicate that these factors don't play a dominant role in well-designed systems.

All calculations so far assume that the detection takes place while the avalanches are still progressing in the gas gap and that avalanches starting too close to the anode don't contribute: only those within a distance g^* of the cathode will be visible. For 0.3 mm gas gaps this distance seems to be about half of the gap and the assumption was confirmed by corresponding Monte-Carlo simulations [36].

In this region it will be deposited an average number of clusters λg^*, Poisson-distributed (73), and the stochastic part of the avalanche growth will be described by (71). The equivalent $P(\mathcal{N}_0)$ will be the compounding ([37] v.1, pp.286, v.2, pp.437) of (73) with (71), with MGF

$$M_{\mathcal{A}+\mathcal{D}}(s) = C_{\mathcal{D}}\left(M_{\mathcal{A}}(s)\right) = \exp\left[r\lambda g^*\left(\frac{r}{r+s}-1\right)\right] \tag{76}$$

Laplace-inversion yields

$$P_{\mathcal{A}+\mathcal{D}}(\mathcal{N}_0) = \mathrm{e}^{-r\lambda g^*}\left[\mathrm{e}^{-r\mathcal{N}_0}\sqrt{\frac{r^2\lambda g^*}{\mathcal{N}_0}}I_1\left(2\sqrt{r^2\lambda g^*\mathcal{N}_0}\right)+\delta(\mathcal{N}_0)\right] \tag{77}$$

PoS(RPC2012)033

where I_1 is the modified Bessel function of first order. The singular term $e^{-r\lambda g^*}\delta(\mathcal{N}_e)$ represents the fundamental Poissonian inefficiency arising from the average number of avalanches $r\lambda g^*$ developing in the region g^*.

If the timing threshold lies below the space-charge regime (see Fig. 16), the function $\mathcal{T}(\mathcal{N}_0)$ can be obtained from $N_{e,th} = N_0 e^{\alpha^* W_e t}$ (see (21)). Expressing $N_{e,th}$ as a time, $N_{e,th} = e^{\alpha^* W_e t_{th}}$ one gets

$$N_0 = e^{\alpha^* W_e (t_{th} - t)} = e^{\tau_{th} - \tau} \tag{78}$$

where, for compactness, it was used the reduced time $\tau = t / (\alpha^* W_e)$. Keeping only the regular part of (77), renormalized to unity, finally it is possible to apply (75):

$$P_{\mathcal{A}+\mathcal{D}}(\mathcal{T}) = u\,\mathrm{e}^{-u} \frac{\sqrt{r\lambda g^*}\, I_1\left(2\sqrt{r\lambda g^* u}\right)}{\left(e^{r\lambda g^*} - 1\right)\sqrt{u}},\ u = e^{\ln(r) + \tau_{th} - \mathcal{T}} \tag{79}$$

A remarkable feature of this distribution is that its shape depends only on $r\lambda g^* = \ln(1-\varepsilon)$, that is, depends only on the fundamental inefficiency of the detector. Keeping this constant, variations of τ_{th} or of r generate only translational movements, so all momenta about the mean $E\left[\left(\mathcal{T} - E(\mathcal{T})\right)^n\right]$ depend only on $r\lambda g^*$. This is also true (on a different variable) if exponentially-distributed cluster statistics is considered [33].

The term $u\,\mathrm{e}^{-u}$ in (79) is a Landau-like distribution corresponding to a single-electron avalanche in the limit $r\lambda g^* \to 0$.

The variance of $\mathcal{T}$ can be calculated as a series [34]

$$\begin{aligned} V_{\mathcal{A}+\mathcal{D}} &= E_{\mathcal{A}+\mathcal{D}}\left[\left(\mathcal{T} - E(\mathcal{T})\right)^2\right] \\ &= \underbrace{\sum_{n=1}^{\infty} W_n\, \zeta(2,n)}_{V_{\mathcal{A}}} + \underbrace{\sum_{n=1}^{\infty} W_n\, \psi^2(n) - \left(\sum_{n=1}^{\infty} W_n\, \psi(n)\right)^2}_{V_{\mathcal{D}}} \end{aligned} \tag{80}$$

$$W_n\left(r\lambda g^*\right) = \frac{\mathrm{e}^{-r\lambda g^*}\left(r\lambda g^*\right)^n}{n!\left(1 - \mathrm{e}^{-r\lambda g^*}\right)}$$

where $\zeta(2,n)$ is the generalized Riemann Zeta function and ψ is Euler's Psi function. The first variance term $V_{\mathcal{A}}$ is related to the avalanche statistics (process $\mathcal{A}$) while the second term

PoS(RPC2012)033

$V_{\mathcal{D}}$ is related to the ionization statistics (process $\mathcal{D}$). The asymptotic behaviour of both terms is $V_{\mathcal{A}} \simeq V_{\mathcal{D}} \simeq 1/\sqrt{r\lambda g^*}$ as shown in Fig. 19.

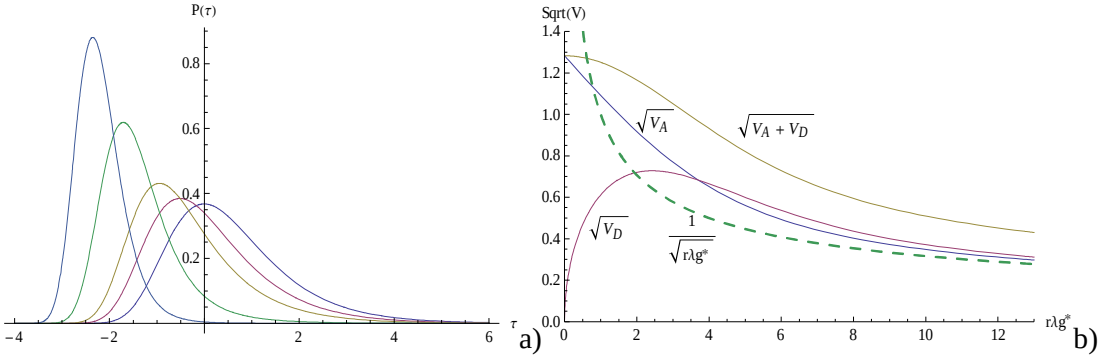

Fig. 19 – a) Representation of the time resolution distribution (79) for $r\lambda g^* = \{0.01,1,2,5,10\}$ and $\tau_{th} = 0, r = 1$ (these produce only translational shifts). b) Standard deviation of the two variance components exposed in (80), along with their quadratic sum and asymptotic behaviour .

Note that the experimental results are normally obtained by a gaussian fit to the experimental distributions and after a number of instrumental corrections such as time-charge correlation, generally producing values that are smaller than those shown in Fig. 19. For a more detailed study see [33].

The inclusion of cluster statistics (process $\mathcal{B}$) increases somewhat the variance and symmetrises $P(\mathcal{T})$, except for exponentially-distributed cluster statistics, which has no effect [33].

In case the discriminating threshold is situated in the space-charge regime (see Fig. 16), (75) and (77) can be used in conjunction with some space-charge model. Using again model (67), the necessary model functions are

$$N_0(\tau) = N_{e,sat}\sqrt[m]{w\left(K'\mathrm{e}^{K'-m\tau}\right)}, \quad K' = \left(N_{e,th}/N_{e,sat}\right)^m$$
$$\left|\frac{\partial N_0}{\partial z}\right| = N_{e,sat}\frac{\sqrt[m]{w\left(K'\mathrm{e}^{K'-m\tau}\right)}}{1+w\left(K'\mathrm{e}^{K'-m\tau}\right)}, \quad \tau = \frac{t}{\alpha W_e} \tag{81}$$

Substitution into (75) is straightforward but produces cumbersome expressions. An example of $P_{\mathcal{A}+\mathcal{D}+space\,charge}(\mathcal{T})$ is presented in Fig. 20. The three leftmost curves correspond to $N_{e,th} < N_{e,sat}$, are regularly spaced and not affected by the value of the parameter m of the space-charge model. The remainder curves lie in the space-charge region and their spacing increases owing to the "saturation" of the charge growth curve as exemplified in Fig. 16, more

PoS(RPC2012)033

so for larger m. Remarkably the variance of the distributions remains essentially unaffected, in agreement with the numerical results (with a different space-charge model) of Lippmann [24].

For the case of single-electron avalanches a similar treatment allowed to calculate analytically the mean and variance of $P_{\mathcal{A}+\mathcal{D}+space\,charge}(\mathcal{T})$ [25], confirming the weak dependence of the variance on $N_{e,sat}$.

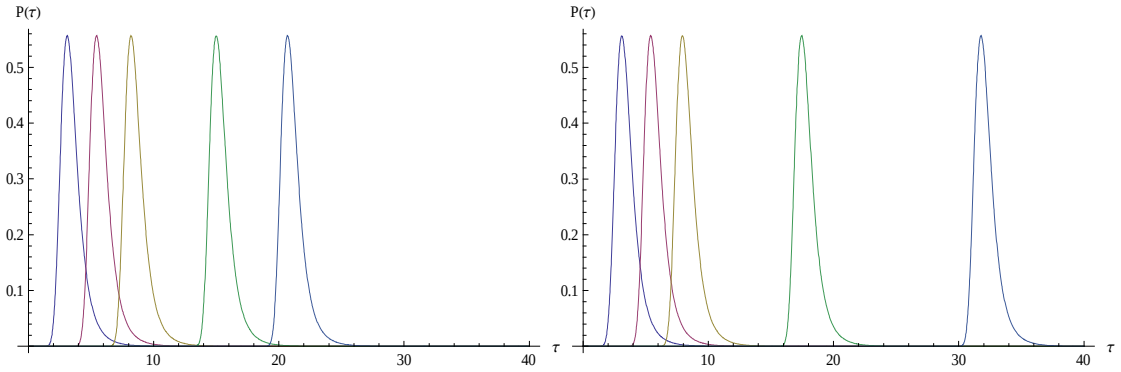

Fig. 20 – Examples of the time distributions obtained with a space-charge model $P_{\mathcal{A}+\mathcal{D}+space\,charge}(\mathcal{T})$. The conditions are $N_{e,sat}=2\times10^4$, $r\lambda g^*=4$, $r=1$, $N_{e,th}=\{10^2,10^3,10^4,10^5,2\times10^5\}$ and $m=\{1,1.5\}$ respectively for the lhs and rhs panels.

5.3. Charge distribution

The charge spectrum generated in RPCs in Townsend avalanche regime have been studied by Monte-Carlo simulation ([23], [39]), but an analytical solution including processes $\mathcal{A}$ to $\mathcal{D}$ was not yet derived. This is possible if cluster statistics is neglected, assuming that all clusters contain a single primary electron [38]. Under this approximation the distribution of the amount of charge created from a single primary electron-ion pair anywhere in the gap is the randomization[1] ([37], v.II, pp.53) of (70) on the uniformly distributed parameter z_0:

$$P_{\mathcal{A}+C}(\mathcal{N}_e)=\int_0^d P_{\mathcal{A}}(\mathcal{N}_e,z_0)\frac{1}{d}dz_0=(1-r)\delta(\mathcal{N}_e)+r\frac{e^{-\mathcal{N}_e r/G}-e^{-\mathcal{N}_e r}}{\mathcal{N}_e\ln(G)} \tag{82}$$

where $G=e^{\alpha^* g}$ is the maximum (cathode-to-anode) average gas gain. The average value is $E_{\mathcal{A}+C}(\mathcal{N}_e)=(G-1)/\ln(G)$. The corresponding MGF is

$$M_{\mathcal{A}+C}(s)=(1-r)+\frac{r}{\ln(G)}\ln\left(\frac{r+s}{r/G+s}\right) \tag{83}$$

[1] Also called mixture or weighting.

PoS(RPC2012)033

The distribution of the total generated charge will be the compounding ([37] v.1, pp.286, v.2, pp.437) of (73) with (83),

$$M_{\mathcal{A}+\mathcal{C}+\mathcal{D}}(s)=C_{\mathcal{D}}\left(M_{\mathcal{A}+\mathcal{C}}(s)\right)=\left(\frac{r+s}{r+Gs}\right)^{m},\qquad m=\frac{\lambda r}{\alpha^{*}} \tag{84}$$

Analytic Laplace-inversion of (84) is only possible for integer m, yielding cumbersome expressions for $P_{\mathcal{A}+\mathcal{C}+\mathcal{D}}(\mathcal{N}_e)$. However, if G is large we may consider the approximation [38]

$$\left(\frac{r+s}{r+Gs}\right)^{m}=\left(\frac{1}{G}+\frac{G-1}{G}\frac{r}{r+Gs}\right)^{m}\underset{G\gg 1}{\approx}G^{-m}+\left(1-G^{-m}\right)\left(\frac{r}{r+Gs}\right)^{m}=\tilde{M}_{\mathcal{A}+\mathcal{C}+\mathcal{D}}(s) \tag{85}$$

which changes the momenta of $\mathcal{N}_e$ by amounts proportional to G^{-m} (which is small for large G and m not too close to zero) but allows analytical inversion, yielding

$$\tilde{P}_{\mathcal{A}+\mathcal{C}+\mathcal{D}}(\mathcal{N}_e)=G^{-m}\delta(\mathcal{N}_e)+\left(1-G^{-m}\right)\left[\frac{e^{\frac{-\mathcal{N}_e}{G/r}}\,\mathcal{N}_e^{\,m-1}\,(G/r)^{-m}}{\Gamma(m)}\right] \tag{86}$$

The term $G^{-m}\delta(\mathcal{N}_e)=e^{-r\lambda g}\delta(\mathcal{N}_e)$ represents the fundamental inefficiency arising from either all avalanches being extinguished by the electronegativity of the gas or the probability that no cluster is produced.

The function in square brakets is the statistical gamma distribution. For $G^{-m}\ll 1$ (small intrinsic inefficiency) the mean and variance arise mostly from this function:

$$\begin{aligned}E(\mathcal{N}_e)&\approx m\frac{G}{r}=\lambda g\frac{G}{\ln(G)}\\ E(\mathcal{N}_e^{\,2})-E(\mathcal{N}_e)^2&\approx m\left(\frac{G}{r}\right)^2\end{aligned} \tag{87}$$

One recognizes that the average generated charge is the average gain from (82) for large G, times the average number of clusters from (73). The relative standard deviation is just $1/\sqrt{m}$. A multigap RPC, where N identical gaps contribute simultaneously to the signal, is equivalent to an increasing λ to λN in a single gap, therefore reducing the relative standard deviation by a factor $1/\sqrt{N}$. An illustration of $\tilde{P}_{\mathcal{A}+\mathcal{C}+\mathcal{D}}(\mathcal{N}_e)$ is shown in Fig. 21 and comparison with data is available in [38].

PoS(RPC2012)033

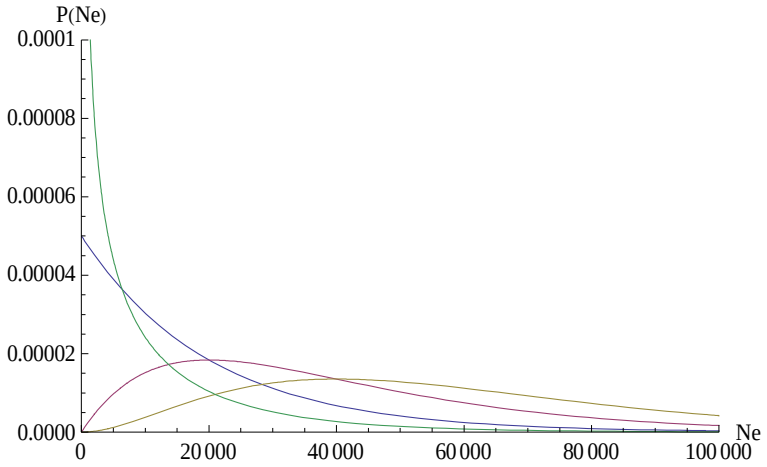

Fig. 21 - Representation of $\tilde{P}_{\mathcal{A}+\mathcal{C}+\mathcal{D}}(\mathcal{N}_e)$ for $G=10^4$, $r=0.5$, $m=\{0.5,1,2,3\}$. Note the very different qualitative behaviour for $m<1$ and $m>1$.

Note that for small $\mathcal{N}_e$ $(\mathcal{N}_e \ll G/r)$, $\tilde{P}_{\mathcal{A}+\mathcal{C}+\mathcal{D}}(\mathcal{N}_e)$ follows a power law: $\tilde{P}_{\mathcal{A}+\mathcal{C}+\mathcal{D}}(\mathcal{N}_e) \sim \mathcal{N}_e^{\,m-1}$. Therefore the parameter $m=r\lambda/\alpha^*$, essentially the ratio between the cluster density and the effective first Townsend coefficient controls qualitatively the behaviour of $\tilde{P}_{\mathcal{A}+\mathcal{C}+\mathcal{D}}(\mathcal{N}_e)$ for small $\mathcal{N}_e$: if $m<1$ the function diverges at origin and it is monotonically decreasing, while for $m>1$ it is null at the origin. This has been already noted in [39].

6. Signal Induction

If the detector comprises only conductors and pure dielectrics, the appearance of currents on the readout electrodes is determined by electrostatic considerations only. However, in RPCs, the presence of materials of non-negligible conductivity strongly complicates the induction process. We will address first the former, simpler, case and then the later one.

6.1. Conductors and dielectrics

The electric field[1] $\vec{E}_q(\vec{r},\vec{r}_q) = -\vec{\nabla}V_q(\vec{r},\vec{r}_q)$ created by each point charge q present in the gas on the position (relative to the electrodes) $\vec{r}_q$ will induce a corresponding surface charge density ς over the surrounding metallic electrodes[2], via the well known relation between the electric field at the surface of a conductor and the underlying surface charge density

[1] Technically the Green's function for the problem, as the field of any charge distribution can be calculated from this by superposition.

[2] Eventually the system of electrodes may not completely enclose the point-charge and some charge may be induced on the gas box or whatever conducting structure surrounds the detector. In the limit the charges may be induced on "the infinite". The case of resistive electrodes will be treated below.

PoS(RPC2012)033

$$\varsigma = \varepsilon \vec{E}_q(surface, \vec{r}_q) \cdot \hat{s} \tag{88}$$

being $\hat{s}$ the unit vector outwardly normal to the conductive surface. Therefore, there will be a current density

$$j_{(ind)} = \frac{d\varsigma}{dt} \tag{89}$$

induced into the surface of the electrodes. The total amount of surface charge induced over each electrode is

$$Q_m(\vec{r}_q) = \iint_{\substack{surface\,of\,the \\ m^{th}\,electrode}} \varsigma(\vec{r}_q)\, ds = qQ'_m(\vec{r}_q) \tag{90}$$

where we have denoted by Q'_m the total surface charge per unit of inducing charge q.

Alternatively, an electrostatic property generally known as Ramo's theorem [40] gives Q_m as

$$Q_m(\vec{r}_q) = -q\frac{V_m(\vec{r}_q)}{V_0} \tag{91}$$

where the potential V_0 is applied to the m^{th} electrode while keeping the other electrodes at null voltage and $V_m(\vec{r}_q)$ is the corresponding potential at the position of the charge, called the "weighting potential". Note that $V_m(\vec{r})$ has no relation to the DC polarization potential but it may be proportional to it in some situations.

Comparing (90) and (91) one can establish the equivalence

$$\begin{aligned} Q'_m(\vec{r}_q) &= -\frac{V_m(\vec{r}_q)}{V_0} \\ \vec{\nabla}_{\vec{r}_q} Q'_m(\vec{r}_q) &= \frac{\vec{E}_m(\vec{r}_q)}{V_0} \end{aligned} \tag{92}$$

between the two views, where we have introduced the weighting field $\vec{E}_m(\vec{r}_q)$, correspondent to the $V_m(\vec{r})$ potential, calculated at the charge position $\vec{r}_q$ and the gradient of Q'_m calculated with respect to the charge position $\vec{r}_q$. In view of this, we may from now on use only one of the views, the equivalence with the other one being given by simple substitution from (92). However it may be noted that the induced current density details revealed by the charge field approach (89) are absent from the weighting field's.

PoS(RPC2012)033

If the electrodes are connected to a low impedance load (otherwise see [41]) the electrode potential may be considered as constant during the induction process. Then, if the charge moves in space between two points $\vec{r}_{q,1} \rightarrow \vec{r}_{q,2}$, across a difference in the weighting potential ΔV_m, the charge that will flow on the external circuit connected to the m^{th} electrode is

$$Q_{m(ind)} = -q\frac{\Delta V_m}{V_0} \tag{93}$$

The rate of variation of the induced charge is the induced current

$$i_m = \frac{dQ_m}{dt} = q\vec{v}_q \cdot \frac{\vec{E}_m(\vec{r}_q)}{V_0} \tag{94}$$

where $\vec{v}_q$ is the velocity of the point charge.

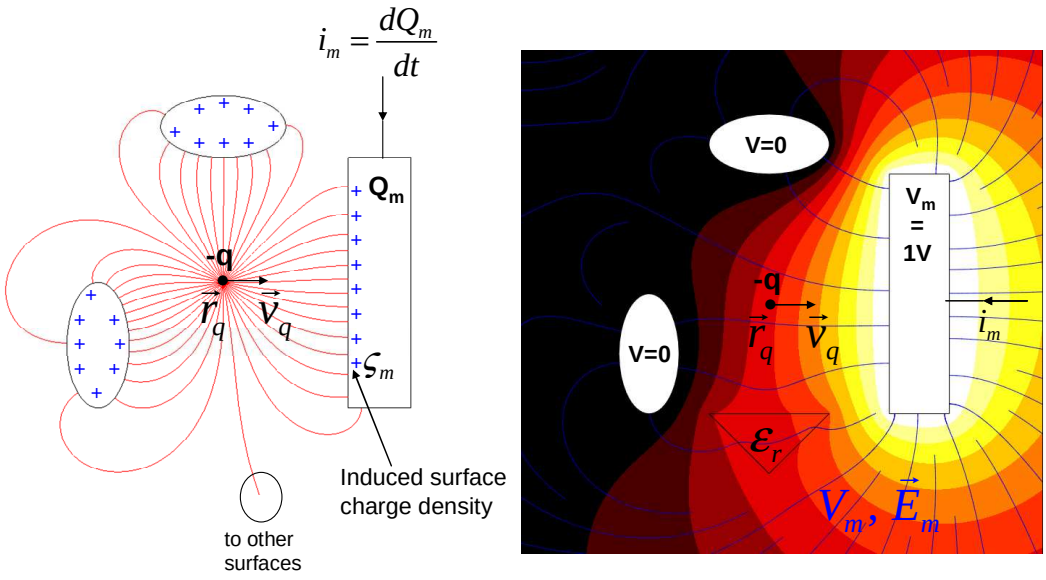

Fig. 22 – Illustration of the two equivalent views on the charge induction process addressed in (90), (91).

To apply (94) to a swarm described by the particle density n and particle flow density $\vec{j}$, one considers a small region of volume dV around the position $\vec{r}$, containing a charge $dq = q_{\pm} n\, dV$ ($q_{\pm}$ being the positive or negative elementary charge, whichever applicable) that moves on average with velocity $\vec{v} = \vec{j}/n$ (see (40)), yielding the current induced per element of volume of the swarm

$$di_m = q_{\pm}\vec{j} \cdot \frac{\vec{E}_m}{V_0} dV \ , \tag{95}$$

PoS(RPC2012)033

which must be integrated to yield the total induced current and charge

$$i_m = \frac{q_\pm}{V_0} \int\limits_{All\ space} \vec{j} \cdot \vec{E}_m \, dV$$
$$Q_{m(ind)} = \int_0^\infty i_m dt \qquad (96)$$

If the weighting field is constant over each gas gap, the induced current calculation may be simplified to

$$i_m = \sum_{All\ gaps} \gamma \int\limits_{gap} \vec{j} \cdot \hat{E}_m \, dV, \qquad \gamma = \frac{q_\pm \left| \vec{E}_m \right|}{V_0} \qquad (97)$$

where the induction factor γ (already mentioned in section 4) is defined and $\hat{E}_m$ is the unit vector in the direction of the weighting field. This expression may be applied also as an approximation.

If the detector comprises only conductors and pure dielectrics, the weighting field is determined by an electrostatic calculation. There are many commercial and academic (for instance [42]) programs capable of performing such calculations.

Analytic solutions are known for some situations. A simple but useful case is the regular multigap RPC with N gas gaps and equally thick resistive plates shown in Fig. 23. The induction factor in this case can be trivially calculated as

$$\gamma = \frac{q_{p^+}}{\underbrace{Ng + \underbrace{\frac{(N+1)d}{\varepsilon_r}}_{\substack{\text{"electrical thickness"} \\ \text{of the plates}}}}_{\text{Total "electrical distance"}}} \qquad (98)$$

which is essentially the elementary charge divided by the “electrostatic thickness” of the RPC, showing that thicker detectors have in induction handicap. For a single gap without dielectrics[1] ($N = 1, d = 0$) the induction factor is maximal: $\gamma = q_{p^+} / g$. The expression can be easily generalized for a non-regular chamber with different gap and electrode widths and different permitivities.

[1] A chamber with metallic electrodes commonly called PPC (Parallel-Plate Chamber).

PoS(RPC2012)033

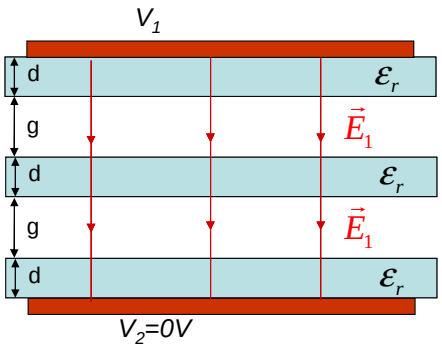

Fig. 23 – Depiction of the weighting field for the top electrode ($m=1$) of a regular multigap RPC with *N=2* gas gaps and uniform external electrodes, corresponding to (98).

In Table 1 there is a list of known analytical or semi-numerical field solutions of interest for RPCs, including charge fields $\vec{E}_q$ and weighting fields $\vec{E}_m$ for strip electrodes. For most cases the solutions are expressed in the form of a series or an integral that must be evaluated numerically.

Table 1 – List of some analytic or semi-numerical solutions of situations of interest for RPCs.

Situation	Quantity	Type of solution	Ref
Single charge between conducting plates filed with an homogeneous permittivity	Potential	Series	[8] v.2, cap III, eq.184
	Potential	Fourier series	[43] (2)
	Potential	Integral	[43] (3)
Voltage strip on a plane condenser filled with homogeneous permittivity	Potential and field	Closed form	[43] (6,7,8) [44]
Gap on a plane condenser filled with homogeneous permittivity	Potential and field	Closed + transcend-dental equations	[44]
Single charge between conducting plates filed with 3 permittivity layers	Potential and field	Integral	[45] (9)
Voltage strip on a plane condenser filled with 3 permittivity layers	Potential and field	Integral	[45] (12,13,14)

6.2. Resistive materials

As the constitutive materials of RPCs (REs and RLs) are not pure dielectrics but have some conductivity, currents will flow on them as the electric fields in their interior change owing to

PoS(RPC2012)033

the movement of the swarm charges. This will, as well, introduce polarization losses in the transmission of the signals towards the amplifiers (see section 7.5).

Although this is a classical subject in detectors (e.g. [46]) it has been recently presented by Riegler [47] a very general theory of signal induction, comprising resistive internal elements and external impedances connected to the electrodes. The basic insight is that one may start with the electrostatic solutions and make the substitution $\varepsilon \to \varepsilon + \sigma / s$, where σ is the materials' conductivity and s a complex frequency. Inverse Laplace transformation $s \to t$ yields the time response for a $\delta(t)$ impulse corresponding to the electrostatic case. One then proceeds by superposition (time-convolution). This procedure is valid both for the induction process itself and for the coupling (now RC-like) between the electrodes.

For instance [48]: a charge distribution $\rho(\vec{r})$ is created at time zero in a conductive homogeneous medium. A single unit charge in a homogenous dielectric (electrostatic solution) will produce the potential $V_{static} = 1/\left(4\pi\varepsilon|\vec{r}|\right)$. Upon substitution and Laplace-inversion the impulse response is

$$V(\vec{r},t) = \frac{1}{4\pi\varepsilon|\vec{r}|}\left(\delta(t) - \frac{e^{-t/\tau}}{\tau}\right), \qquad \tau = \frac{\varepsilon}{\sigma} \tag{99}$$

The parameter τ is the material's relaxation time that already appeared in section 3.2. The solution for the persistent charge distribution $\rho(\vec{r})$ can be constructed by time and space superposition:

$$\begin{aligned} V_\rho(\vec{r},t) &= \int_{All\ space} \int_0^t V(\vec{r}-\vec{r}',t-t')\,\rho(\vec{r}')\,\theta(t')\,dt'\,dV \\ &= e^{-t/\tau}\,\frac{1}{4\pi\varepsilon}\int_{All\ space} \frac{\rho(\vec{r}')}{|\vec{r}-\vec{r}'|}\,dV \end{aligned} \tag{100}$$

This is just the classical electrostatic solution multiplied by an exponential decay factor, arising because the charges in the material flow until the internal electric field is cancelled.

As another example, (94) becomes

$$i_m = \frac{q}{V_0}\int_0^t \vec{v}_q(t')\cdot\vec{E}_m(\vec{r}_q(t'),t-t')\,dt' \tag{101}$$

The current at the present time will depend on the charge position and velocity at times past, weighted by the time-dependent weighting field obtained by applying an impulse $V_0\delta(t)$ to the m^{th} electrode and using the Laplace transform procedure mentioned above.

Several interesting cases are treated in [47], [48]. The behaviour-defining quantity is the materials' relaxation time $\tau = \varepsilon/\sigma$. For phenomena of typical duration $T << \tau$ (such as $\delta(t)$

PoS(RPC2012)033

impulses…) the materials behave as pure dielectrics and for the opposite case $T >> \tau$ as good conductors. In the intermediate cases there can be relaxation and diffusion-like phenomena. To give orders of magnitude, permittivities are typically around $10\,pF/m$ and bakelite conductivity around $10^{-7}\,S/m$ [1] resulting in $\tau \approx 1ms$, to be compared with typical electron transit times of tens of nanoseconds and ion transit times of tens of microseconds. It is clear that for the most common materials likely the conductivity of the REs plays no relevant role.

However, the RLs, or special electrodes for high counting rates, may have much higher conductivity, which introduce additional phenomena. To illustrate this behaviour we will use the result in [45] eq. 71 to calculate a representative case: the influence of a bidimensional RL on the charge density (88) induced by a point charge q (positive ion for instance) that moves from a metallic anode up to the RL in the time lapse T, as depicted in Fig. 24. For simplicity, all materials were considered as having the same permittivity ε, as this doesn't vary much among most common materials, and the RL was collapsed to a bidimensional layer with surface resistivity $\Re$.

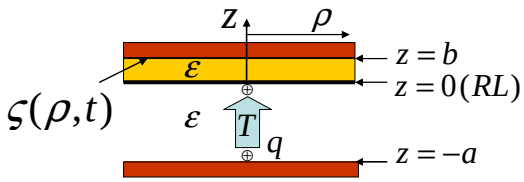

Fig. 24 – Representation of the situation treated as an example of the phenomena arising from the introduction of a RL of non-negligible conductivity in RPCs.

A sketch of the calculation is given in Appendix II. The solution can be expressed in terms of the dimensionless variables

$$\begin{aligned} &a' = a/(a+b),\ \rho' = \rho/(a+b),\ \varsigma' = \varsigma(a+b)^2/q, \\ &t' = t/\tau,\ T' = T/\tau,\ \tau = \varepsilon\Re(a+b), \end{aligned} \tag{102}$$

which highlight the fundamental physical dependencies. In Fig. 25 it is shown a graphical representation of the reduced induced charge density ς' as a function of t' for $a' = 0.8,\ T' = \{0,1\}$ and several radial distances from the axis. For comparison, the $\Re = 0$ case is also plotted. The induced current density is (89) the time-derivative of this curve. The induced charge eventually visible in the acquisition electronics is the induced charge density ς, integrated over whatever electrode shapes there will be in the surface (90) and time-weighted by the shaping of the front-end electronics (not included in this calculation), which typically limits the "observation time" over which the charge is collected, essentially defining where in the time axis in Fig. 25 the value of the induced charge should be taken.

[1] Glass conductivity is much lower, around $10^{-11}\,S/m$

PoS(RPC2012)033

The fundamental behaviour is that for $t' \ll 1$ the RL has little influence on the induction process, corresponding to the charge transparency situation. Otherwise, there is over time a transfer of induced charge from the axis towards the periphery (which will be visible if the electronics shaping time is long enough) in a wavelike pattern. In the limit of very long time ($\sim t' > 10$) the induced charge will be almost uniformly spread over the whole surface. If $T' \sim 1$ or larger the full induced charge cannot be collected close to the axis, as it will be transferred away before the induction process ends.

The charge transfer process resembles the diffusion-like process that would take place in a bidimensional RC network fed by the induction current density (e.g [46], [49]), but the formal equivalence hasn't been investigated.

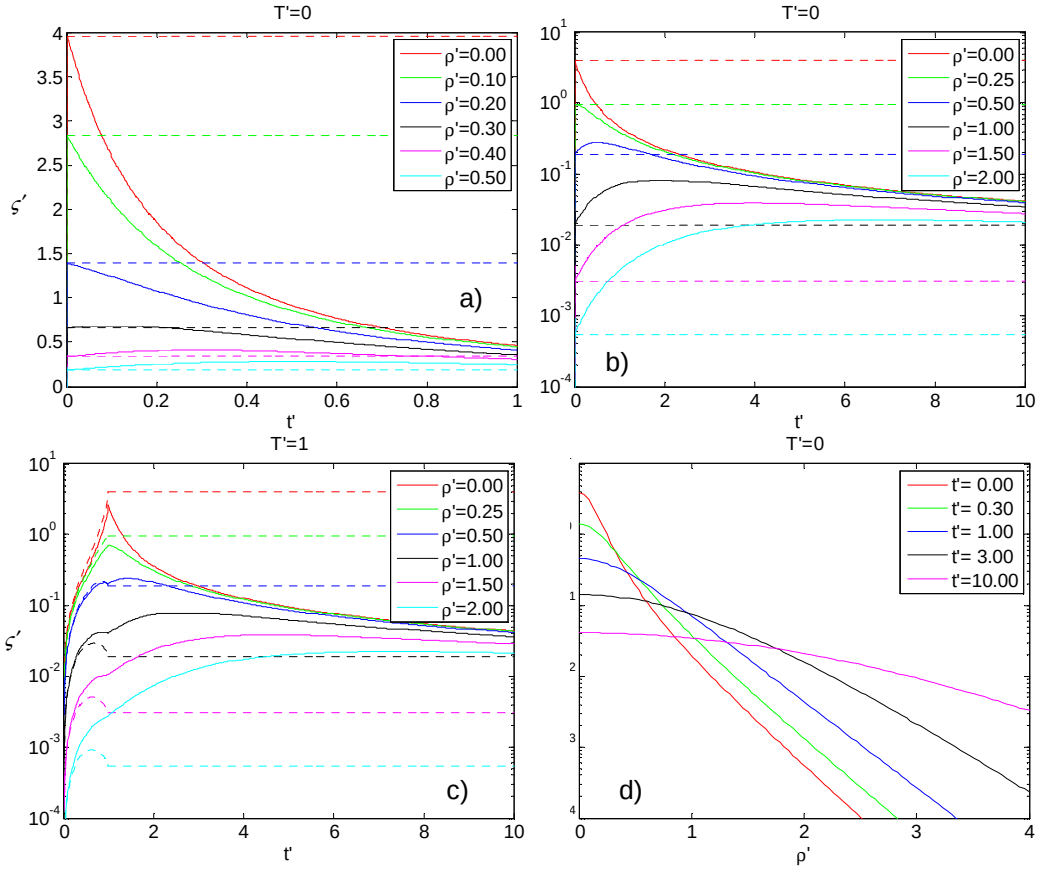

Fig. 25 – a) to c) Reduced induced charge density ς' as a function of t' for $a' = 0.8$, $T' = \{0,1\}$ and several radial distances from the axis (see Fig. 24 and (102)). For comparison, the $\Re = 0$ case is also plotted (dashed lines). The induced current density into the surface is the time-derivative of these curves, resembling [48], figure 9. d) ς' as a function of ρ' for different times. (In this case the $\Re = 0$ and $t' = 0$ cases coincide.) There is over time a transfer of induced charge from the axis towards the periphery in a diffusion-like pattern.

PoS(RPC2012)033

The shape of the electrodes plays a role as well, as the charge-spreading effect is stronger close to the induction axis. A similar calculation for strip electrodes is given in [48] (see also Appendix II).

7. Signal transmission

The charge induction process injects a current into the readout electrodes, which must then be transmitted towards the amplifiers. This is particularly important for timing RPCs, which use a narrow gas gap that generates a very fast signal upon which a precise time is eventually measured.

Naturally, there is an infinity of possible electrode arrangements. The most common cases are arrays of rectangular pads or a set of parallel strips. The first question is whether such conductor structures should be treated as multiconductor transmission lines (MTL) or just as circuit nodes. The general rule is that when the structures are "electrically large", larger than the smallest significant wavelength of the signal, should be treated as transmission lines. Estimates [50] point to lengths of 80 cm for 2 mm gap RPCs and 5 cm for 0.3 mm gap RPCs.

While for the case of strips (translationally invariant structures in one dimension) there is a well developed theory (e.g. [51], [52]) no work is known for the case of large pads. However, we will discuss below that also the standard MTL theory is likely inaccurate for widespread structures such as RPCs as it misses the fact that the strips are quite separated in space and that there must be some propagation velocity across the strips as well, which will limit the formation of fully organized propagation modes.

7.1. Frequency spectrum

As stated above, to decide how to treat the problem it is important to know the signals' frequency spectrum.

Even if this is not exact owing to the space-charge effect, as a coarse guide we may calculate the Fourier transform of (43). Neglecting the second term within the square brackets, which, being negative, must not be dominant, taking a fixed width in the erf term, equal to the width of the avalanche when the swarm centre encounters the anode, and allowing negative t the following approximation is produced

$$\underset{\sim}{I}_{e(ind)} \simeq \tilde{\underset{\sim}{I}}_{e(ind)}(t) = \frac{1}{2}\gamma W_e \exp\left(\alpha^* W_e t\right)\left(1+erf\left(\frac{z_0 - vt}{2\sqrt{D_e z_0 / v}}\right)\right), \tag{103}$$

A Fourier transform calculation yields

$$\left|\tilde{\underset{\sim}{I}}_{e(ind)}(\omega)\right| = K\frac{1}{\sqrt{\omega^2 + W_e^2 \alpha^{*2}}}\exp\left(-\omega^2 \frac{D_e z_0}{v^3}\right) \tag{104}$$

PoS(RPC2012)033

where $\omega = 2\pi f$ is the angular frequency. Apart from scale factors represented by K, one recognizes a pole at $\omega = W_e \alpha^*$, clearly related to the gas amplification process. This is multiplied by a Gaussian, related to the diffusion coefficient. In Fig. 26 both $\tilde{I}_{e(ind)}$ and $\left|\tilde{I}_{e(ind)}(\omega)\right|$ are represented for two values of D_e, a realistic one and, for comparison, a very short one corresponding to an almost diffusionless situation. There two cutoff frequencies[1]: $f_{c1} = W_e \alpha^* / (2\pi)$ is associated with the amplification process and $f_{c2} = \sqrt{\frac{\ln(2) v^3}{2 D_e z_0}} \Big/ 2\pi$ is associated with the diffusion process. For the values used in this figure $f_{c1} = 580\,MHz$ and $f_{c2} = 860\,MHz$.

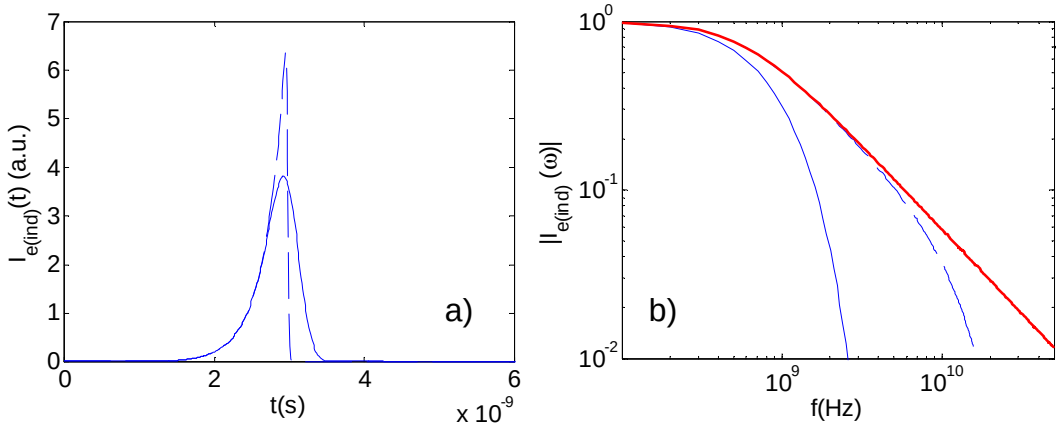

Fig. 26 – a) Representation of $\tilde{I}_{e(ind)}$ for the same parameters used in Fig. 10 (solid line) and with D_e reduced by a factor 100 (dashed line). b) The blue line corresponds to $\left|\tilde{I}_{e(ind)}(\omega)\right|$ normalized to unity at low frequencies, for the two D_e cases studied. The red curve corresponds to the pole at $\omega = W_e \alpha^*$.

7.2. Signal transmission in stripline electrodes

The general theory of MTLs has been particularized for the case of RPCs in [53] and further developed in [50]. The signal is injected in a single strip (or more if we proceed by superposition) by a current source. The problem is rather complex and there are many possible situations of interest. In here we will follow the view represented in Fig. 27, as it captures the essence of the problem.

[1] Defined, as usual, as the frequency at which the attenuation associated with the corresponding term is 1/√2.

PoS(RPC2012)033

7.3. General theory

In here we will outline only the most fundamental formulas and results. The interested reader may consult the vast bibliography on the subject (e.g. [50]-[54]) for details.

The system consists of $N+1$ translationally invariant electrodes, including one reference ("ground") electrode. The currents in the strips and the strip-to-ground and termination-to-ground (at $x=0$) voltages are denoted by the $N\times 1$ vectors $\mathbf{I}(x,t)$, $\mathbf{V}(x,t)$ and $\mathbf{V}_T(t)$. A current pulse $I_0(x_0,t)$ is injected from the ground into a single ("driven") strip at position x_0, propagating in both directions along x and coupling to the neighbouring strips (crosstalk). The strips have length D and are terminated by resistor networks (or just the input impedance of the amplifiers) at $x=0$ and $x=D$. These terminations don't need to be equal and can be extended to handle general linear networks and interconnections with other MTLs [54].

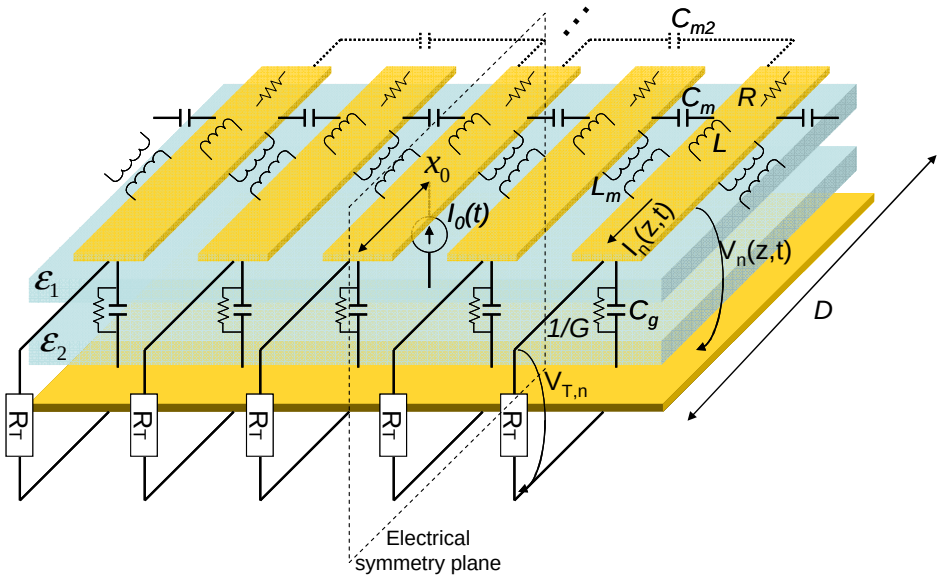

Fig. 27 – Representation of the geometry and the most relevant quantities for the problem of propagation in a microstrip array, along with the main simplifications.

The electrical properties are summarized in the $N\times N$ per unit length capacitance, inductance, resistance and conductance matrices, respectively $\mathbf{C},\mathbf{L},\mathbf{R},\mathbf{G}$. In general these are symmetric matrices and all conductors will couple to each other via the diagonal elements, but later we will particularize for "weak-coupling" approximations.

If all materials involved have magnetic permeability close to vacuum's, the inductance matrix can be calculated from the capacitance matrix $\mathbf{C}_0$ obtained with all dielectrics removed

PoS(RPC2012)033

$$\mathbf{L} = \mathbf{C}_0^{-1} / c^2 , \tag{105}$$

c being the speed of light in the vacuum. Therefore, all parameters can be obtained by electrostatic[1] calculations only. In case the medium is homogeneous (not an RPC…) with relative permittivity ε_r then

$$\mathbf{L} = \frac{\mathbf{C}^{-1}}{c^2 / \varepsilon_r} = \frac{\mathbf{C}^{-1}}{v^2} \tag{106}$$

where v is the speed of light in the medium. This has important consequences, as in this case there are no "propagation modes".

The fundamental equations to be satisfied are

$$\begin{aligned} \frac{\partial^2 \mathbf{V}}{\partial z^2} - \mathbf{LC}\frac{\partial^2 \mathbf{V}}{\partial t^2} &= \mathbf{RGV} + (\mathbf{RC} + \mathbf{LG})\frac{\partial \mathbf{V}}{\partial t} \\ \frac{\partial^2 \mathbf{I}}{\partial z^2} - \mathbf{CL}\frac{\partial^2 \mathbf{I}}{\partial t^2} &= \mathbf{GRI} + (\mathbf{CR} + \mathbf{GL})\frac{\partial \mathbf{I}}{\partial t} \end{aligned} \tag{107}$$

The most remarkable feature of the signal transmission in MTLs (except in the case (106)) is the existence of propagation modes. Each mode consists in certain fixed ratios of currents in the electrodes that propagate ensemble at the same velocity. For N electrodes there are N modes, each propagating with its characteristic modal velocity v_m, leading to the phenomenon of modal dispersion. The ensemble of the modes forms a basis of the space of all possible current patterns, so any desired initial current pattern will excite a certain number of modes with certain amplitudes and will disperse in accordance with the corresponding combination of modal velocities.

In the time domain, modal analysis is possible only in the lossless case, vanishing the RHS of (107). The solution of the problem is [50]

$$\begin{aligned} \mathbf{V}_T(t) = \frac{\mathbf{1} + \mathbf{\Gamma}_0}{2} \sum_{j=0}^{\infty} (\mathbf{\Gamma}_D \mathbf{\Gamma}_0)^j \times \\ \left(\mathbf{Z}_c \mathbf{M} \begin{bmatrix} M_{1n}^{-1} I_0\left(t - \dfrac{x_0 + 2jD}{v_1}\right) \\ \vdots \\ M_{Nn}^{-1} I_0\left(t - \dfrac{x_0 + 2jD}{v_N}\right) \end{bmatrix} + \mathbf{\Gamma}_D \mathbf{Z}_c \mathbf{M} \begin{bmatrix} M_{1n}^{-1} I_0\left(t - \dfrac{2(j+1)D - x_0}{v_1}\right) \\ \vdots \\ M_{Nn}^{-1} I_0\left(t - \dfrac{2(j+1)D - x_0}{v_N}\right) \end{bmatrix} \right) \end{aligned} \tag{108}$$

[1] The steady current calculations needed to calculate **R** and **G** are essentially the same as for electrostatics.

PoS(RPC2012)033

In here, j denotes the order of the successive reflections, n is the driven strip, $\mathbf{\Gamma}_0$ and $\mathbf{\Gamma}_D$ are the voltage reflection matrices at each end of the chamber given by

$$\mathbf{\Gamma}_{0,D} = \left(\mathbf{Z}_{0,D} - \mathbf{Z}_c\right)\left(\mathbf{Z}_{0,D} + \mathbf{Z}_c\right)^{-1}, \tag{109}$$

where $\mathbf{Z}_c$ is the characteristic impedance matrix that relates the currents and voltages in the strips, $\mathbf{V}(x,t) = \mathbf{Z}_c\mathbf{I}(x,t)$, and $\mathbf{Z}_{0,D}$ the termination matrix in each end of the chamber. Note that if $\mathbf{Z}_{0,D} = \mathbf{Z}_c$ the reflection matrices vanish and there are no reflections. This requires all strips to be interconnected to each other by resistors with adequate values. In practice, second-neighbour connections may suffice [53].

In case there is just a simple, uniform, termination to ground in each strip in both ends, then $\mathbf{Z}_{0,D} = \mathbf{1}R_T$ ($\mathbf{1}$ is the unitary matrix), $\mathbf{\Gamma}_0 = \mathbf{\Gamma}_D = \mathbf{\Gamma} = \mathbf{1} - \mathbf{T}$, the solution can be written in a more compact way [50]

$$\mathbf{I}_T(t) = \frac{\mathbf{V}_T(t)}{R_T} = \frac{\mathbf{T}}{2}\sum_{j=0}^{\infty}\left(1-\mathbf{T}\right)^j \mathbf{M}\begin{bmatrix} M_{1n}^{-1} I_0\left(t - \dfrac{(-1)^j x_0 + 2[j/2]D}{v_1}\right) \\ \vdots \\ M_{Nn}^{-1} I_0\left(t - \dfrac{(-1)^j x_0 + 2[j/2]D}{v_N}\right) \end{bmatrix} \tag{110}$$

$$\mathbf{T} = 2\mathbf{Z}_c\left(\mathbf{1}R_T + \mathbf{Z}_c\right)^{-1}$$

where $\lceil j/2 \rceil$ represents the next higher integer of $j/2$.

The columns of the modal current matrix $\mathbf{M}$ ($\mathbf{M}_m$) represent the current ratios that correspond to each mode and are the N solutions of the eigenvalue problem

$$\mathbf{CLM}_m = \frac{1}{v_m^2}\mathbf{M}_m \tag{111}$$

which is obtained by replacing the usual *ansatz* $\mathbf{I} = \mathbf{I}(t \pm x/v_m)$ in the (lossless) 2nd eq. (107).

The values $M_{m,n}^{-1}$ are the elements of $\mathbf{M}^{-1}$ and correspond to the amount of excitation needed in each mode (m) to reproduce the current injection at strip n boundary condition $\mathbf{I}(z_0,t) = \left[0,\cdots,I_0(t),\cdots,0\right]^T$ (see [53]). The modal excitation is such that the modes interfere destructively over all strips except the n^{th}. After some propagation length the modes will loose coherence owing to their different propagation velocities (modal dispersion) and the destructive interference is mitigated, leading to increased signals in the neighbouring strips. Potentially, after a sufficient long propagation length, each mode (typically spanning most of the strips) may

PoS(RPC2012)033

be observed at the terminations separated in time from the other modes. This causes modal crosstalk, to be discussed later in more detail.

The characteristic impedance matrix is given by

$$\mathbf{Z}_c = \mathbf{LMvM}^{-1} \tag{112}$$

with

$$\mathbf{v} = \begin{bmatrix} v_1 & 0 & 0 \\ & \ddots & \\ 0 & 0 & v_N \end{bmatrix} \tag{113}$$

This theory has been compared in some detail with measurements in RPC-like situations and a good agreement has been generally found [50], [53].

The same theory can be formulated in the frequency domain (see [52] for instance). In this case the *ansatz* is $\mathbf{I} = \mathbf{I}(\omega)\mathrm{e}^{i\omega t}\, e^{\pm\gamma_m x}$. The input and output quantities are the Fourier time-transforms of the signals and the equations (107) become

$$\begin{aligned} &\gamma_m^2 \mathbf{V}(\omega) = \mathbf{ZYV}(\omega) \\ &\gamma_m^2 \mathbf{I}(\omega) = \mathbf{YZI}(z,\omega) \\ &\mathbf{Z} = \mathbf{R} + i\omega\mathbf{L},\ \mathbf{Y} = \mathbf{G} + i\omega\mathbf{C} \end{aligned} \tag{114}$$

proceeding the solution more or less along the same lines. In general, the modal propagation factors $\gamma_m(\omega)$ are complex numbers, expressing losses in the real part (exponential attenuation along x) and the modal propagation velocity in the imaginary part:

$$\gamma_m = \alpha_m(\omega) + i\frac{\omega}{v_m(\omega)} \tag{115}$$

Although less intuitive, this approach has the advantage that it is possible to include losses and the frequency dependency of the materials and that all reflections are automatically taken into consideration in the output without need for iterations. Indeed, replacing the harmonic *ansatz* in (108), one sees that the sum over the reflections forms a power series that can be summed for each mode:

$$\begin{aligned} \mathbf{V}_T(\omega) = I_0(\omega)\frac{\mathbf{1}+\boldsymbol{\Gamma}_0}{2}\sum_{m=1}^{N} M_{m,n}^{-1}\left[\mathbf{1}-\boldsymbol{\Gamma}_D\boldsymbol{\Gamma}_0\,\mathrm{e}^{-\gamma_m 2D}\right]^{-1}\times \\ \left[\left(\mathbf{Z}_c\mathbf{M}\right)_m \mathrm{e}^{-\gamma_m x_0} + \left(\boldsymbol{\Gamma}_D\mathbf{Z}_c\mathbf{M}\right)_m \mathrm{e}^{-\gamma_m(2D-x_0)}\right] \end{aligned} \tag{116}$$

PoS(RPC2012)033

A very important practical characteristic is the amount of interstrip coupling (crosstalk), given by $V_{T,m}/V_{T,n}$. This can be readily calculated numerically and general guidelines [53] seem to be that simple termination (no interconnections), lower amplifier input impedances and longer shaping times help reduce crosstalk.

There are two contributing factors to this behaviour. For short counters, those for which the difference in propagation time between modes is small (including relevant reflections), that is, the modes remain coherent, crosstalk is determined just by the structure of the $\mathbf{T}$ matrix. This can be seen from (110): neglecting reflections $(j=0)$ and disregarding the differences between the modal propagation velocities it becomes just $\mathbf{I}_T(t)=\frac{\mathbf{T}}{2}[0,...,I(t-x_0/v),...0]^T$.

As the counters become long, extra phenomena of interference/decoherence between modes becomes important, as shown, for instance, in [50] fig. 8, [53] fig. 7. This will be discussed in the next section.

For optimization purposes, an analytical solution for these problems would be very useful, but this seems to be prohibitive in the general case because of the eigenvalue calculation (111). However, progress can be made in weak-coupling approximations.

7.4. Weak-coupling approximations

In a planar structure such as depicted in Fig. 27 it is clear that the direct coupling from a strip to its second neighbour, represented by c_{m2}, will be much smaller than to its nearest neighbour and may be neglected. For instance, the values given in [50] table 2 indicate that $C_m/C\approx 1/10$, $C_{m2}/C_m \ll 1/10$. Furthermore, realistic numerical examples [50], [53], suggest that the nearest-neighbour coupling strength is relatively weak, on the order of 10%. This suggests a number of simplifications that yield analytical solutions.

7.4.1. Feed-forward

The most radical approximation to weak-coupling is to modify the fundamental equations to neglect the back-interaction between the neighbouring and the driven strips [55] along with all direct coupling between the driven and all other strips except the first neighbours. This leads to constitutive matrices with the structure (giving as an example a 5-strip system, driven on strip 3)

PoS(RPC2012)033

$$\mathbf{C}=\begin{bmatrix} C & -C_m & 0 & 0 & 0 \\ 0 & C & -C_m & 0 & 0 \\ 0 & 0 & C & 0 & 0 \\ 0 & 0 & -C_m & C & 0 \\ 0 & 0 & 0 & -C_m & C \end{bmatrix},\ \mathbf{L}=\begin{bmatrix} L & L_m & 0 & 0 & 0 \\ 0 & L & L_m & 0 & 0 \\ 0 & 0 & L & 0 & 0 \\ 0 & 0 & L_m & L & 0 \\ 0 & 0 & 0 & L_m & L \end{bmatrix} \qquad (117)$$

$$C = C_g + C_m$$

In this approximation the driven strip behaves as a single conductor transmission line which induces signals in the neighbouring strips without being affected by them. The solution proceeds in cascade from the driven strip, so there are no modes and only strip pairs need to be considered. The solution for an externally driven stripline, corresponding to an avalanche close to one end of an RPC, is given in [55]. In particular it is shown that the signal induced in the neighbouring line is proportional to the time derivative of the driven line's.

7.4.2. Nearest neighbour

A step further from the feedforward approximation would be to consider only interactions between nearest neighbours, neglecting c_{m2}. In this approximation the capacity matrix becomes (a symmetric tridiagonal Toeplitz – STT – matrix)

$$\mathbf{C}=\begin{bmatrix} C & -C_m & 0 & 0 & \\ -C_m & C & -C_m & 0 & \cdots \\ 0 & -C_m & C & -C_m & \\ 0 & 0 & -C_m & C & \\ & \vdots & & & \ddots \end{bmatrix} \equiv \begin{Bmatrix} C & -C_m \\ -C_m & C \end{Bmatrix} = C \begin{Bmatrix} 1 & -u \\ -u & 1 \end{Bmatrix} \qquad (118)$$

$$C = C_g + C_m, \quad u = C_m / C$$

As most of this section will deal with such type of matrices these will be represented in curly braces. The results will not depend on the size of the matrix and indeed the matrices between curly braces correspond to a 2-strip system under the same approximations.

Requiring additionally $u = C_m / C \ll 1$ (weak coupling), all expressions will be developed in series of u and truncated to the first order. This renders all matrices STT, as the elements further removed from the main diagonal are quadratic in u.

Besides $\mathbf{C}$ we need the capacitance matrix with all dielectrics removed

$$\mathbf{C}_0 = C_0 \begin{Bmatrix} 1 & -u_0 \\ -u_0 & 1 \end{Bmatrix} \qquad (119)$$

and from these all relevant quantities can be calculated.

PoS(RPC2012)033

$$\mathbf{L} = L\begin{Bmatrix} 1 & \frac{L_m}{L} \\ \frac{L_m}{L} & 1 \end{Bmatrix} = \frac{1}{c^2 C_0}\begin{Bmatrix} 1 & u_0 \\ u_0 & 1 \end{Bmatrix} \tag{120}$$

$$\mathbf{CL} = \frac{C}{c^2 C_0}\begin{Bmatrix} 1 & u_0 - u \\ u_0 - u & 1 \end{Bmatrix}. \tag{121}$$

The inverse squared modal velocities and the modal currents are the eigenvalues and the eigenvectors of $\mathbf{CL}$ (111). For an STT matrix $A = \begin{Bmatrix} b & a \\ a & b \end{Bmatrix}$ of size N there are simple analytical expressions for these [56]:

$$\lambda_m = b + 2a\cos\left(\frac{m\pi}{N+1}\right),\ M_{k,m} = \sqrt{\frac{2}{N+1}}\sin\left(\frac{km\pi}{N+1}\right),\ m,k = 1,2,...,N \tag{122}$$

Furthermore, $\mathbf{M}$ is unitary: $\mathbf{M}^{-1} = \mathbf{M}$. For instance, a 5×5 system yields

$$\boldsymbol{\lambda} = b + \begin{bmatrix} a\sqrt{3} \\ a \\ 0 \\ -a \\ -a\sqrt{3} \end{bmatrix},\ \mathbf{M} = \begin{bmatrix} \frac{\sqrt{3}}{6} & \frac{1}{2} & \frac{\sqrt{3}}{3} & \frac{1}{2} & \frac{\sqrt{3}}{6} \\ \frac{1}{2} & \frac{1}{2} & 0 & -\frac{1}{2} & -\frac{1}{2} \\ \frac{\sqrt{3}}{3} & 0 & -\frac{\sqrt{3}}{3} & 0 & \frac{\sqrt{3}}{3} \\ \frac{1}{2} & -\frac{1}{2} & 0 & \frac{1}{2} & -\frac{1}{2} \\ \frac{\sqrt{3}}{6} & -\frac{1}{2} & \frac{\sqrt{3}}{3} & -\frac{1}{2} & \frac{\sqrt{3}}{6} \end{bmatrix} \tag{123}$$

Because of the unitarity of $\mathbf{M}$, the columns represent the current ratios for each mode and simultaneously the amount of excitation of each mode when the strip corresponding to a column is driven. If this is the central strip it can be seen that all odd modes are excited[1] with equal amplitudes and the central mode inverted.

Taking into consideration (121) and (122), the modal velocity spectrum is contained within

$$1 - |u_0 - u| \approx \frac{1}{\sqrt{1 + 2|u_0 - u|}} < \frac{v_m}{c\sqrt{\frac{C_0}{C}}} < \frac{1}{\sqrt{1 - 2|u_0 - u|}} \approx 1 + |u_0 - u| \tag{124}$$

[1] All even modes are zero for the center strip, so can't contribute. The modes are clearly related to the Fourier series.

PoS(RPC2012)033

If $u_0 = u$, indicating a dielectrically homogeneous or compensated ([57], [58]) system, the spectrum collapses to a single velocity and there are no modes.

In a 2-strip system there are the modal velocities

$$\mathbf{v} = \overline{v}\begin{bmatrix} 1+\dfrac{\Delta v}{2\overline{v}} \\ 1-\dfrac{\Delta v}{2\overline{v}} \end{bmatrix} = c\sqrt{\frac{C_0}{C}}\begin{bmatrix} 1+\dfrac{u_0-u}{2} \\ 1-\dfrac{u_0-u}{2} \end{bmatrix}, \tag{125}$$

spanning half of the maximum spectral width and reproducing eq. (5) of [58].

Curiously, within the weak-coupling approximations, the structure of the characteristic impedance matrix $\mathbf{Z}_c$ doesn't depend on the details of the modal structure and the calculation proceeds as

$$\mathbf{Z}_c = Z_c\begin{Bmatrix} 1 & \dfrac{Z_m}{Z_c} \\ \dfrac{Z_m}{Z_c} & 1 \end{Bmatrix} = \frac{1}{c\sqrt{C_0 C}}\begin{Bmatrix} 1 & \dfrac{u+u_0}{2} \\ \dfrac{u+u_0}{2} & 1 \end{Bmatrix} \tag{126}$$

$$\mathbf{1}-\boldsymbol{\Gamma}_0 = \mathbf{T} = T\begin{Bmatrix} 1 & \dfrac{T_m}{T} \\ \dfrac{T_m}{T} & 1 \end{Bmatrix} = \frac{2}{w+1}\begin{Bmatrix} 1 & \dfrac{w}{w+1}\dfrac{u+u_0}{2} \\ \dfrac{w}{w+1}\dfrac{u+u_0}{2} & 1 \end{Bmatrix},\ w = \frac{R_T}{Z_c} \tag{127}$$

which reproduces as well the 2-strip results of [58] equations (6), (7), (11). Actually, within these approximations, the only information gained in going beyond a 2-strip model is the knowledge of the modal structure (122). It is clear that there will be crosstalk also to second-neighbours, etc, but in the present approximation this is quadratically (cubically, etc), smaller and it is excluded from the expressions. It can be readily appreciated that the coupling crosstalk (T_m / T) decreases with R_T (if $R_T < Z_c$), u and u_0. Taking $u \approx u_0 \approx 0.1$, $R_T \approx 2Z_c$ this should be around 7%, as it is actually found in [50] Fig.15 (exact, compensated curves).

A complementary form of crosstalk arises from modal dispersion. This is owed to the decoherence of the modes that initially interfere destructively at the injection point (x_0) of the current I_0. Taking the example of a 5-strip system (123) it can be seen that with, for instance, signal injection at strip 3, substantial excitation arises in all odd modes (values in column 3) and that these modes span all strips (values in colums 1, 3, 5). Therefore, if there is full decoherence, replicas of the injected signal (eventually inverted and/or scaled), corresponding to the individual modes, will be seen separated in time (see [53] figure 7 for instance) and will span

PoS(RPC2012)033

the full width of the counter regardless of how wide it is. The modes have no locality property! This is likely unphysical because there must be a lateral propagation velocity as well, which was not at all taken in consideration in the present theory. Given this, and in absence of a fuller theory, a 2-strip model is likely more realistic for a wide RPC than the N-strips'.

Neglecting reflections (which actually decohere more as they travel longer before reaching the terminations) the 2-strip solution is, after (110),

$$\mathbf{I}_T(t) = \frac{1}{4}\begin{bmatrix} T & T_m \\ T_m & T \end{bmatrix}\begin{bmatrix} I_0\left(t-\frac{x_0}{v_1}\right)+I_0\left(t-\frac{x_0}{v_2}\right) \\ I_0\left(t-\frac{x_0}{v_1}\right)-I_0\left(t-\frac{x_0}{v_2}\right) \end{bmatrix}. \tag{128}$$

The relative time delay between both modes per unit of the propagation length x_0 is, taking in consideration (125),

$$\frac{\Delta t}{x_0} = \frac{\Delta v}{\bar{v}^2} = \frac{|u-u_0|}{c\sqrt{\frac{C_0}{C}}}. \tag{129}$$

Replacing data from [50] table 2 (uncomp), this is on the order of 0.15 to 0.25 ns/m. Considering a signal $I_0(t)$ with duration of ~2 ns (e.g. from Fig. 10), the modes will completely decohere after about a 10 m propagation length. However, significant modal crosstalk when compared with coupling crosstalk (from $\mathbf{T}$ matrix) is already visible for 2 m lengths ([50], fig 15), underlining the importance of modal compensation (making $u = u_0$). It is also clear that a slow shaping in the electronics will increase the effective signal width and improve the situation, as suggested in [53].

In the frequency domain, for some frequencies there will be a phase inversion of one mode with respect to the other, destructive interference will turn into constructive and constructive into destructive, yielding the crosstalk peak and transmission dip shown in [50] Fig. 8 c).

7.5. Losses

Resistive losses arise from the series resistance of the electrodes. As the current is not supposed to flow sideways, the $\mathbf{R}$ matrix must be diagonal.

Conductivity losses, to be expressed in $\mathbf{G}$, arise from conductivity in the dielectrics, interconnecting the electrodes or these to ground, and from polarization losses that arise from the rearrangement of charges within dielectrics in response to electric field changes. In uniform dielectrics both conductivities are proportional to the capacity matrix [50], but it is unlikely to be so in non-homogeneous structures. Indeed, losses have been measured in a glass RPC and were found to have a more complex behaviour, with cut-off frequency about 1 GHz [50].

PoS(RPC2012)033

The treatment of losses must be performed in the frequency domain following the formulation (114). In the general case the solution must be performed numerically [54], but we may argue that for the case of RPCs some approximations may be workable.

For a single strip the constitutive matrices become scalars and from (114) it is obvious that

$$\Gamma = \sqrt{YZ} = \sqrt{(R + i\omega L)(G + i\omega C)} \tag{130}$$

which, to the first order in R, G (low-loss approximation) yields

$$\Gamma \approx -\frac{RC + LG}{2\sqrt{LC}} + i\omega\sqrt{LC} \tag{131}$$

emphasizing the attenuation coefficient and the propagation velocity (compare with (115)).

The solution of (114) under the same low-loss plus the weak-coupling approximations described above reaches similar conclusions: the same, mode-independent, attenuation coefficient (131) and unchanged modal velocities and modes (122).

Acknowledgement

To Alessio Mangiarotti for very useful opinions and clarifications and to Stefano Bianco for being an encouraging and tolerant editor.

This work was financed by the Portuguese Government through FCT-Foundation for Science and Technology and FEDER/COMPETE under the contracts CERN/FP/116392/2010, CERN/FP/123605/2011.

References

[1] C. Grupen, *Particle Detectors*, Cambridge Monographs on Particle Physics, Cambridge University Press (1996)

[2] K. Kleinknecht, *Detectors for Particle Radiation*, Cambridge University Press (1998)

[3] D. Green, *The Physics of Particle Detectors*, Cambridge Monographs on Particle Physics, Cambridge University Press (2000)

[4] F. Sauli, *Principles of operation of multiwire proportional and drift chambers*, CERN-77-09 (1977)

[5] L. Lopes et al. Nucl. Phys. B (Proc. Suppl.) 158 (2006) 66-70 (DOI: 10.1016/j.nuclphysbps.2006.07.017)

[6] L. Naumann et al., Nucl. Instrum. and Meth. A 635 supp.1 (2011) S113-S116 (DOI: 10.1016/j.nima.2010.09.121)

[7] J. Wang, et al., Nucl. Instr. and Meth. A 621(2010)151

[8] E. Durand, *Électrostatique*, Masson et C^{ie}, Paris (1964)

[9] A. Blanco et al., Nucl. Instrum. and Meth. A 508 (2003) 70

PoS(RPC2012)033

[10] E. Cerron-Zeballos et al., Nucl Instrum. and Meth. A 374 (1996) 132

[11] C. Lippmann et al., Nucl. Phys. B (Proc. Suppl.) 158 (2006) 127

[12] M. Abbrescia, Nucl Instrum. and Meth. A 533 (2004) 7

[13] D. González-Díaz et al, Nuclear Physics B (Proc.Suppl.) 158 (2006) 111

[14] J.M. Meek and J.D. Craggs (1953), "Electrical Breakdown of Gases", Clarendon Press, Oxford, 1953

[15] J.A. Rees (edit.) (1973), "Electrical Breadown of Gases", The MacMillan Press, Ltd., London

[16] M.M. Fraga et al., Nucl Instrum. and Meth. A 323 (1992) 284

[17] A.J. Davies and C.J. Evans, The Theory of Ionization Growth in Gases Under Pulsed and Static Fields, CERN 73-10 (1973)

[18] J. Brambring, Zeitchrift für Physic 179 (1964) 532-538

[19] A.L. Ward, J. Appl. Phys. 36 (1965) 1291 (doi:10.1063/1.1714297)

[20] J. de Urquijo et al., Eur.Phys.J.D 51 (2009) 241–246

[21] M. Abbrescia et al., Nuclear Physics B (Proc. Suppl.) 78 (1999) 459-464

[22] P.Fonte, Nucl. Instrum. and Meth. A456 (2000) 6-10

[23] W.Riegler et al., Nucl. Instrum. and Meth. A500 (2003) 144–162

[24] C. Lippmann,W. Riegler, Nucl. Instrum. and Meth. A517 (2004) 54–76

[25] A.Mangiarotti et al., Nuclear Physics B (Proc.Suppl.) 158 (2006) 118–122

[26] H. Raether, *Electron Avalanches and Breakdown in Gases*, Butterworths, 1964

[27] P. Fonte, IEEE Trans. Nucl. Sci. 43:3 (1996) 2135

[28] G. Aielli et al., Nucl. Instrum. and Meth. 508 (2003) 6–13

[29] P. Fonte and V. Peskov, Nucl. Instrum. and Meth. A477 (2002) 17–22

[30] R.M. Corless et al., Adv.Comp.Math. 5 (1996) 329

[31] W. Riegler et al., Nucl. Instrum. and Meth. A 500 (2003) 144–162

[32] A. Mangiarotti, private communication

[33] W. Riegler, Nucl. Instrum. and Meth. A 602 (2009) 377–390

[34] A. Mangiarotti et al., Nucl. Instrum. and Meth. A 533 (2004) 16–21

[35] I.B. Smirnov, Nucl. Instrum. and Meth. A 554 (2005) 474-493

[36] A. Blanco et al., Nucl. Instrum. and Meth. A A513 (2003) 8–12

PoS(RPC2012)033

[37] W. Feller, *An Introduction to Probability Theory and Its Applications*, J. Willey & Sons, N.Y. (1970)

[38] P. Fonte, *Calculation of the charge spectrum generated by ionizing particles in Resistive Plate Chambers at low gas gain*, arXiv:1211.1743 [physics.ins-det]

[39] M. Abbrescia et al., Nucl. Instrum. and Meth. A 431 (1999) 413-427

[40] S. Ramo, Proc. IRE 27 (1939) 584

[41] E. Gatti et al., Nucl. Instrum. and Meth. A 193 (1982) 651-653

[42] N. Majumdar et al., Nucl. Instrum. and Meth. A 602 (2009) 719-722

[43] T. Heubrandtner et al., Nucl. Instrum. and Meth. A 489 (2002) 439-443

[44] B. Schnizer et al., Nucl. Instrum. and Meth. A 535 (2004) 554-557

[45] T. Heubrandtner et al., *Static Electric Fields in an Infinite Plane Condensor with One or Three Homogeneous Layers*, CERN-OPEN-2001-074 (2002)

[46] G. Battistoni et al., Nucl. Instrum. and Meth. 202 (1982) 459-464

[47] W. Riegler, Nucl. Instrum. and Meth. A 535 (2004) 287–293

[48] W. Riegler, Nucl. Instrum. and Meth. A 491 (2002) 258–271

[49] S. Dixit et al., Nucl. Instrum. and Meth. A 518 (2004) 721–727

[50] Diego Gonzalez-Diaz et al., Nucl. Instrum. and Meth. A 648 (2011) 52-72

[51] C.R. Paul, IEEE Trans. Electron. Comput. 44(3) (2002) 413

[52] A.R. Djordjević et al., Proceedings of the IEEE 75:6 (1987) 743-764

[53] W. Riegler and D. Burgarth, Nucl. Instrum. and Meth. A 481 (2002) 130–143

[54] A.R. Djordjević and T.K.Sarkar, IEEE Trans. on Microwave Th. And Tech. 35:10 (1987) 898-908

[55] C.R. Paul, IEEE Trans. on Electromag. Compat. 44:3 (2002) 413-423

[56] D.K. Salkuyeh, International Mathematical Forum,1:22 (2006) 1061-1065

[57] D.M. Pozar, *Microwave Engineering*, 2nd ed. John Wiley & Sons, Inc (1998), section 7.6, pp 393

[58] D.Gonzalez-Diaz, Nucl. Instrum. and Meth. A 661 (2012) S172–S176

PoS(RPC2012)033

Appendix I

$$\underset{\sim}{n}_{i+}(z,t)=\iint\limits_{\substack{radial\\plane}}\Bigg(\underbrace{\int\limits_{\substack{longi-\\tudinal}}\iint\limits_{\substack{radial\\plane}}\Bigg(\underbrace{\int\limits_0^\infty \underbrace{e^{-\frac{\rho'^2}{f(t')}}g(z',t')}_{\alpha\vec{j}_{i+}\cdot\hat{W}_{i+}}dt'}_{n_{i+}(\vec{r},0)}\Bigg)\Bigg(\underbrace{e^{-\frac{(\rho-\rho')^2}{f'(t)}}g'(z-z',t)}_{h_{i+}(\vec{r},t)}\Bigg)d\rho'dz'}_{\underset{\sim}{n}_{i+}(\vec{r},t)}\Bigg)d\rho$$

$$=\int\limits_{\substack{longi-\\tudinal}}\Bigg[\underbrace{\int\limits_0^\infty\Bigg(\iint\limits_{\substack{radial\\plane}}\Bigg(\iint\limits_{\substack{radial\\plane}}e^{-\frac{\rho'^2}{f(t')}}e^{-\frac{(\rho-\rho')^2}{f'(t)}}d\rho'\Bigg)d\rho\Bigg)}_{\pi^2 f(t')f'(t)}g(z',t')dt'\Bigg]g'(z-z',t)dz' \quad (132)$$

$$=\pi^2\int\limits_{\substack{longi-\\tudinal}}\Bigg[\underbrace{\int\limits_0^\infty f(t')g(z',t')dt'}_{n_{i+}(z,0)}\Bigg]\underbrace{f'(t)g'(z-z',t)}_{h_{i+}(z,t)}dz'$$

Appendix II

Making the substitutions $\varepsilon_2\to\varepsilon+\sigma/s=\varepsilon+1/(\Re gs)$, $\varepsilon_1=\varepsilon_3=\varepsilon$, $q=a, p=b$, and then taking the limit $g\to 0$ in [45] eq. 71, yields (88) the surface charge induced by a point charge Q in the position $-a\le z_0\le 0$ over the surface of the top electrode $(z=b)$

$$\varsigma(z_0,s)=-\frac{Q}{\pi}\varepsilon\Re s\int_0^\infty dk\,\frac{\left(e^{kz_0}-e^{-k(2a+z_0)}\right)e^{-kb}kJ_0(k\rho)}{\left(e^{-2kb}+e^{-2ka}\right)k+\left(2\varepsilon\Re s-k\right)e^{-2k(a+b)}-\left(2\varepsilon\Re s+k\right)} \quad (133)$$

where J_0 is the Bessel function of first kind and zeroth order. Upon Laplace inversion, the response to a $Q\delta(t)$ impulse is

PoS(RPC2012)033

$$\varsigma'(z_0',t') = \varsigma\frac{(a+b)^2}{Q}$$
$$= \int_0^\infty \frac{dk'}{a+b}\frac{-2f_1\delta(t') + f_0 k' \exp\left(-\frac{f_0 k' t'}{2f_1}\right)}{\pi\varepsilon\Re f_1^2}\times \quad (134)$$
$$\sinh\left((a'+z_0')k'\right)\mathrm{e}^{(-k')}k' J_0(k'\rho')$$
$$f_0 = 2\mathrm{e}^{2k'(q'-1)} + 2\mathrm{e}^{-2k'q'} - 2\mathrm{e}^{-2k'} - 2;\ \ f_1 = 2\mathrm{e}^{-2k'} - 2$$
$$z_0' = z_0/(a+b);\ a' = a/(a+b);\ \rho' = \rho/(a+b);$$
$$t' = t/\left(\varepsilon\Re(a+b)\right);\ k' = k(a+b)$$

Dimensionless variables, indicated by a prime, where introduced to highlight the basic physical dependencies.

The transportation of the charge Q in the gap $-a' \le z_0' \le 0$ with uniform velocity during the time lapse $T' = T/\left(\varepsilon\Re(a+b)\right)$ and then standing still at $z_0 = 0$ can be calculated by superposition

$$\varsigma'(t') = \varepsilon\Re(a+b)\int_0^{t'}\varsigma'(-(1-u/T')a', t'-u)\theta(T'-u)du + \quad (135)$$
$$\varepsilon\Re(a+b)\int_0^{t'}\varsigma'(0,t'-u)\theta(u-T')du$$

where the factor $\varepsilon\Re(a+b)$ appears because the integral is being calculated in t'. This yields the final result

$$\varsigma'(t'<T') = \int_0^\infty dk' \frac{4f_0T'\left[\cosh\left(\frac{k'a't'}{T'}\right) - \exp\left(-\frac{k'f_0t'}{2f_1}\right)\right] + 8f_1a'\sinh\left(\frac{k'a't'}{T'}\right)}{\left(2f_1a'\right)^2 - \left(f_0T'\right)^2}\times$$
$$\frac{e^{-k'}k'a'J_0(k'\rho')}{\pi}$$
$$\varsigma'(t'\ge T') = \int_0^\infty dk' \frac{4f_0T'\left[\cosh(k'a') - \exp\left(-\frac{k'f_0T'}{2f_1}\right)\right] - 8f_1a'\sinh(k'a')}{\left(2f_1a'\right)^2 - \left(f_0T'\right)^2}\times \quad (136)$$
$$\frac{\exp\left(-k'\left(\frac{(t'-T')f_0}{2f_1}+1\right)\right)k'a'J_0(k'\rho')}{\pi}$$

PoS(RPC2012)033

This should be compared with the behaviour when $\Re \to 0$,

$$\varsigma'_{\Re=0}(t' \le T') = \int_0^\infty dk' \frac{\sinh\left(\frac{k'a't'}{T'}\right)e^{-k'}}{\pi f_1} k'J_0(k'\rho') \qquad (137)$$

$$\varsigma'_{\Re=0}(t' \ge T') = \int_0^\infty dk' \frac{\sinh(k'a')e^{-k'}}{\pi f_1} k'J_0(k'\rho')$$

Note: the calculation of the total charge induced in strip electrodes from expressions such as (136) is not difficult because the required integral over the surface of the electrode can be done analytically

$$\int_0^X \int_{-\infty}^{\infty} J_0(k\sqrt{x^2+y^2})\,dydx = \frac{2\sin(kX)}{k^2} \qquad (1.138)$$

remaining the integral in k to be performed numerically.

PROCEEDINGS OF SCIENCE

Index

PoS(RPC2012)033

PROCEEDINGS OF SCIENCE

